6.27.98

Radar Observations of Asteroid 7822 (1991 CS)

LANCE A. M. BENNER, STEVEN J. OSTRO, KEITH D. ROSEMA, JON D. GIORGINI, DENNIS CHOATE, RAYMOND F. JURGENS, RANDY ROSE, MARTIN A. SLADE, MICHAEL L. THOMAS, RON WINKLER, AND DONALD K. YEOMANS

Jet Propulsion Laboratory, California Institute of Technology, Pasadena, CA 91109-8099
E-mail: lance@think.Jpl.Nasa.Gov

Author	AC	voice	fax	JPL mailstop	E-mail
Benner	818	354-7412	354-9476	300-233	lance@think.jpl.nasa.gov
Ostro	818	354-3173	354-9476	300-233	ostro@echo.jpl.nasa.gov
Rosema	818	393-2629	354-9476	300-233	rosema@think.jpl.nasa.gov
Giorgini	818	393-3107	393-1159	301-150	jdg@tycho.jpl.nasa.gov
Yeomans	818	354-2127	393-1159	301-150	Donald.K.Yeomans@jpl.nasa.gov
Choate	760	255-8358	255-8354	DSCC-61	Dennis.Choate@jpl.nasa.gov
Jurgens	818	354-4974	354-6825	238-420	jurgens@bvd.jpl.nasa.gov
Rose	760	255-8259	255-8515	DSCC-61	rose@intruder.gdscc.nasa.gov
Slade	818	354-2765	354-6825	238-420	marty@shannon.jpl.nasa.gov
Thomas	818	393-3085	354-9476	300-233	wart@echo.jpl.nasa.gov
Winkler	760	255-8259	255-8515	DSCC-61	winkler@intruder.gdscc.nasa.gov

27 manuscript pages (or 16 excluding tables and figure captions)
10 figures, 8 tables
Keywords: asteroids, radar, 1991 CS

Proposed running head: Radar observations of 1991 CS

Correspondence address:

Dr. Lance A. M. Benner

Mail Stop 300-233

Jet Propulsion Laboratory

California Institute of Technology

4800 Oak Grove Drive

Pasadena, CA 91109-8099

E-mail: lance@think.jpl.nasa.gov

ABSTRACT

We report Doppler-only (cw) radar observations of 1991 CS obtained at Goldstone at a transmitter frequency of 8510 MHz (3.5 cm) on 1996 August 26, 27, 28 and 29. Weighted, optimally filtered sums of cw echoes achieve signal-to-noise ratios in excess of 300 per day that thoroughly cover the asteroid in rotation phase (synodic period = 2.39 h, obtained photometrically by Pravec *et al.*, submitted). A weighted sum of all cw spectra gives an OC radar cross section of 0.24 ± 0.08 km^2 and a circular polarization ratio of 0.28 ± 0.001. Our observations place up to fifty 0.98-Hz resolution cells on 1991 CS at echo powers greater than two standard deviations of the noise. Variations of ~10 Hz in the echo's 2-sigma bandwidth are evident on each day and are consistent with the rotation period. Inversion of echo edge frequencies yields convex hulls of the pole-on silhouette for each day. The hulls have a mean elongation and rms dispersion of 1.18 ± 0.02 and place a lower bound on the maximum pole-on dimension of 1.3 km/cosδ, where δ is the angle between the radar line-of-sight and the asteroid's pole direction (which is unknown). The hulls suggest that 1991 CS has the least elongated pole-on silhouette of any of the eight near-Earth asteroids for which similar shape information from radar observations is available. If we assume that the projected area of 1991 CS is the same as that of a sphere with a diameter of 1.1 km, equal to the lower bound on the minimum breadth of the pole-on silhouette on August 28 and 29, then 1991 CS' radar cross section and absolute magnitude of 17.5 correspond to upper limits on the radar and optical geometric albedos of 0.25 and 0.14 that are consistent with its S-class taxonomy. The circular polarization ratio and radar albedo do not vary substantially as a function of rotation phase, suggesting that the near-surface of 1991 CS is relatively uniform. Among the nineteen S-class asteroid radar detections previously reported, the circular polarization ratio of 1991 CS is greater than eleven, comparable to four, and less than five.

INTRODUCTION

Near-Earth asteroid 7822 (1991 CS) approached within 0.051 AU of Earth on 1996 August 28, its closest terrrestrial encounter since 1971 and until 2065. 1991 CS was discovered on 1991 February 11 by R. S. McNaught and K. S. Russell (1991), but prior to the 1996 encounter, the physical properties of this object were effectively unknown. Photometry of 1991 CS by Pravec *et al.* (1998) yielded a synodic rotation period of 2.39 hours and a maximum lightcurve amplitude of ~0.3 magnitudes. R. P. Binzel (personal communication) and M. D. Hicks (personal communication) found that 1991 CS' visible-near infrared spectrum is indicative of the S taxonomic class. Table I summarizes the asteroid's physical properties.

We observed 1991 CS at Goldstone in August 1996. Optimally filtered, weighted sums of echo power spectra achieve signal-to-noise ratios per date in excess of 300. The observations reveal that 1991 CS is a modestly asymmetric object with a maximum pole-on dimension of about 1.3 km and that it has the least elongated pole-on silhouette among the radar-observed NEAs for which similar information is available.

OBSERVATIONS

Our observation and reduction techniques are similar to those described by Mitchell *et al.* (1995) and Ostro *et al.* (1992, 1996). Each observing cycle (run) consisted of transmission of a circularly polarized wave for close to the expected round-trip light travel time to the target, followed by reception of echoes for a comparable duration. In Doppler-only or continuous wave (cw) observations, echoes were received simultaneously in the opposite (OC) and same (SC)

senses of circular polarization as the transmission.

Our reduction of raw data included background removal, calibration, and the formation of sums of spectra. In our spectra, echo power in units of standard deviations of the noise is plotted versus Doppler frequency relative to the Doppler location of the target's estimated center of mass (COM). Echo power is given by $P_R = P_T G_T G_R \lambda^2 \sigma/(4\pi)^3 R^4$, where P_T is the transmitted power, G_T and G_R are the antenna's gain during transmission and reception, λ is the wavelength (3.52 cm at the Goldstone transmitter frequency of 8510 MHz), and R is the target's distance. The radar cross section σ, which is 4π times the backscattered power per steradian per unit flux incident at the asteroid, is estimated by integrating Doppler-only echo power spectra. Uncertainties in σ are dominated by systematic pointing and calibration errors; due to the strength of the 1991 CS echoes, we assign standard errors of 35% to the radar cross section.

The circular polarization ratio $\mu_C = \sigma_{SC}/\sigma_{OC}$ is a gauge of near-surface roughness at spatial scales within about an order of magnitude of the radar wavelength (Ostro 1993). For μ_C, systematic effects cancel and most remaining statistical errors propagate from receiver noise according to Fieller's theorem (Kendall and Stuart 1979, pp. 136-138; Ostro *et al.* 1992). Another useful intrinsic property is the OC radar albedo

$$\hat{\sigma}_{OC} = \sigma_{OC}/A = 4\sigma_{OC}/\pi D_{eff}^2 \qquad (1)$$

where A is the target's projected area and the effective diameter D_{eff} is the diameter of a sphere with the same projected area as the target.

Echo power spectra represent one-dimensional images that can be thought of as brightness scans through a slit parallel to the target's apparent spin vector. The echo's instantaneous bandwidth B is

$$B = 4\pi D(\phi) \cos\delta/(\lambda P) \qquad (2)$$

where D is the breadth of the plane-of-sky projection of the pole-on silhouette at rotation phase ϕ, P is the apparent rotation period, λ is the radar wavelength, and δ is the angle between the radar line-of-sight and the object's apparent equator. If P is known, then measuring B and setting $\cos\delta = 1$ places a lower bound on the asteroid's maximum pole-on breadth D_{max}. Expressing B in Hz, D in kilometers, and P in hours gives $B = 99.7\ D(\text{km})\cos\delta/P(\text{hrs})$ at $\lambda = 3.52$ cm.

Our ability to discern the echo's bandwidth depends on the signal-to-noise ratio, the target's shape, the radar scattering law, and the frequency resolution. Using our previous experience with modeling asteroid echoes as a guide, we adopt an estimator that measures spectral edge frequencies at the points above and below the estimated COM frequency where the echo power first drops to two standard deviations (Benner *et al.* 1997).

We observed 1991 CS on 1996 August 26, 27, 28, and 29, dates that straddled its closest approach to Earth (Table II). The echoes were expected to be strong enough for delay-Doppler imaging, but a problem with the delay-Doppler data acquisition system restricted the observations to Doppler-only on each day. The duration of the observing tracks and the asteroid's short rotation period yielded thorough rotation phase phase coverage (Fig. 1) on each day and limited gaps in rotation phase coverage on any day to less than ~35°.

RESULTS

Figure 2 shows 0.98-Hz resolution echo power spectra from each day and Table III summarizes 1991 CS' disc-integrated radar properties. The OC radar cross sections and circular polarization ratios on each day are consistent within their standard errors and yield: $\sigma_{OC} = 0.24 \pm 0.08$ km^2 and $\mu_C = 0.28 \pm 0.001$. Among the twenty S-class main-belt and near-Earth asteroid radar

detections previously reported, the circular polarization ratio of 1991 CS is greater than eleven, comparable to four, and less than five (Ostro *et al.* 1985, Ostro *et al.* 1991b, Benner *et al.* 1997, Ostro *et al.* 1998), indicating that 1991 CS has a near-surface that is somewhat more rough at decimeter spatial scales than the average radar-detected S-class asteroid.

Figure 3 shows grayscale images of raw resolution OC echo power spectra as a function of time (rotation phase) for each day. Pixels in each row show an echo power spectrum in standard deviations from one run, so that time (rotation phase) increases from top to bottom and Doppler frequency increases from left to right. Displaying echo power spectra in this format highlights bandwidth variations and facilitates searches for brightness features moving across the spectra as the target rotates. The maximum two-sigma bandwidths increase from 41 Hz on August 26 to 50 Hz on August 28 (Table III), indicating that the line of sight moved toward the equatorial plane during the experiment. The bandwidth on August 29 is nearly the same as that obtained on August 28, suggesting comparable subradar latitudes on both days. Bandwidth variations of ~10 Hz that correlate with rotation phase are evident in spectra obtained on each day and are consistent with the rotation period obtained by Pravec *et al.* (1998). We experimented with different contrast stretches, saturation levels, and phase and frequency smoothing combinations but did not find any brightness features rotating through the spectra.

Figure 4 shows spectra smoothed to 10° rotation phase intervals on each day. The spectra show shape variations such as spikes on either side of 0 Hz and flat spectral tops as a function of rotation phase. The thorough rotation phase coverage led us to search for recurring features at the same phases on multiple rotations on each day and on subsequent days, but with the exception of bandwidth variations, we did not find evidence for any.

Figure 5 compares OC spectra that were obtained on opposite sides of the asteroid on

August 27, 28, and 29. Each spectrum is smoothed to frequency and rotation phase resolutions of 4 Hz and 30°. To facilitate comparison of the spectra, we scaled the weaker spectrum to the peak SNR of the stronger spectrum and then we subtracted spectra obtained between 180° and 359° from those obtained between 0° and 179°. The differenced spectra have statistically significant ~10-15 sigma peaks at their negative edges and comparably strong troughs at their positive edges that indicate edge shifts of several Hz. The spectra are also somewhat asymmetric and have approximately mirror symmetry in their shapes. These signatures are consistent with a modest shape asymmetry and a subradar latitude within a few tens of degrees of the target's equator.

Figures 6 and 7 show single-run OC and SC echo power and μ_C versus rotation phase for each day. The OC and SC echo powers are nearly flat on August 26, but subtle variations of about ± 10% in the OC cross section that correlate positively with bandwidth variations as a function of rotation phase (cf. Fig. 3) are evident on the other three days. In Fig. 7, variations of a few tens of percent in μ_C are evident that are probably due to noise in the estimates, but in general, the lack of systematic variations in the circular polarization ratio suggest the near-surface roughness of 1991 CS is relatively uniform as a function of rotation phase.

Figure 8 shows 1991 CS' ecliptic positions during the observations, an interval in which the asteroid moved ~40°. As noted above, the progression of bandwidths during the experiment suggests that the subradar latitude was approaching the equator between August 26 and 28. Hoping to improve constraints on the pole direction, we did a grid search of all possible pole directions at 5° intervals, using the maximum 2-sigma bandwidths for each day, 1991 CS' ephemeris, and a range of maximum pole-on breadths between 1.2 and 1.5 km, but we found that the differences in the bandwidths and the relatively limited sky motion were insufficient to provide useful bounds on the pole direction. Our constraints on the pole direction will improve substantially with a suc-

cessful detection during the asteroid's next close approach in 2015, when 1991 CS will be ~150° from its position in late August of 1996.

SHAPE AND COMPOSITION

Hull estimation

Given sufficient rotational coverage and SNR, measurements of echo edge frequencies can be used to obtain the convex hull of the target's pole-on silhouette (Ostro *et al.* 1988, 1990a). The convex hull can be thought of as the shape of a rubber band stretched around the pole-on silhouette of the asteroid. The fundamental idea of this technique is that the difference between the positive edge and center-of-mass frequencies in an echo power spectrum is proportional to the distance between the approaching limb and the plane that contains the apparent spin vector and the radar line of sight. The "support function" $p(\phi) = p_+(\phi) = p_-(\phi + 180°)$ is a periodic function of rotation phase and satisfies $p(\phi) + p''(\phi) = r(\phi)$, where $r(\phi)$ is the hull's radius of curvature (which is ≥ 0 because the hull is convex) at its approaching limb and primes indicate differentiation with respect to ϕ. Cartesian coordinates of the hull are given by $x(\phi) = p(\phi) \cos(\phi) - p'(\phi) \sin(\phi)$ and $y(\phi) = p(\phi) \sin(\phi) + p'(\phi) \cos(\phi)$.

We estimated convex hulls as follows. We smoothed the spectra in frequency to resolutions of 2, 4, and 8 Hz, and for each frequency resolution, we smoothed the spectra in rotation phase to resolutions of 10, 20, and 30°. We added synthetic echo spectra representing a Lambertian sphere with the same radar cross section (and a comparable bandwidth) as the asteroid to the spectra at three different center frequencies that did not overlap the echoes from the asteroid, which yielded synthetic spectra that were contaminated with noise. For each frequency/phase smoothing combination, we estimated edge frequencies of the synthetic spectra using detection thresholds between

0 and 3 standard deviations in intervals of 0.5 standard deviations. We used weighted least squares to fit a 10th-order Fourier series to the edges of the synthetic spectra and identified the frequency/phase smoothing and edge estimator combinations that reproduced the Lambert sphere model the best, and then we applied those frequency/phase smoothing and edge estimator combinations to estimate the data vector $\mathbf{p}_{dat}$ of edge frequencies for the asteroid's echoes. We repeated this process for echoes from each day. We used weighted least squares again to fit a 10-harmonic Fourier model $\mathbf{p}_{unc}$ to $\mathbf{p}_{dat}$, then we found another Fourier model $\mathbf{p}_{con}$ that was constrained to have positive radii of curvature and to be as close as possible to $\mathbf{p}_{unc}$. We repeated this process for a large enough range of center frequency values to locate the minimum value of the weighted sum of squares of the residuals χ^2.

Table IV lists the Doppler offsets obtained from the hull estimation. This astrometry was entered into JPL's On Site Orbital Determination (OSOD) program and was used to generate a new orbital solution (#6, Table V) that is also available on the Internet at the JPL Solar System Dynamics website at: http://ssd.jpl.nasa.gov/radar_data.html/ (Chamberlin *et al.* 1997). The 1996 radar astrometry shrinks the 1-sigma plane-of-sky error ellipse area at the time of 1991 CS' next close encounter in 2015 by ~50%.

Figure 9 shows our hull estimates for each day and Table VI lists key hull parameters. The hulls are modestly asymmetric and are elongated along an axis displaced by approximately +30° relative to our assigned zero rotation phase. The hulls establish lower bounds on the minimum and maximum pole-on dimensions of 1.1 and 1.3 km/cosδ on August 28 and 29 and have a mean elongation and rms dispersion of 1.18 ± 0.02. Elongations that have been reported for seven other radar-detected NEAs (Table VII) have a mean and rms dispersion of 2.1 ± 0.5 with a minimum of 1.4 for 6178 (1986 DA), demonstrating that 1991 CS has the least elongated pole-on silhouette of

any NEA for which similar shape information from radar observations is available. The modest elongation of 1991 CS' pole-on silhouette is also consistent with the 0.2-0.3 magnitude lightcurve amplitude observed by Pravec *et al.* (1998) in August 1996 and March 1997.

In principle, the relative rotational orientation of the hulls on each day could constrain the sense of rotation if the hulls were sufficiently elongated, the SNR were high enough, and if the sky motion were sufficiently large. We overlaid the hulls to search for orientation changes but we did not find compelling evidence to constrain the sense of rotation.

Composition

Figure 10 shows how the radar and optical geometric albedos of 1991 CS depend on its effective diameter. The figure also indicates representative values of p_v for principal taxonomic classes and condenses information about the distribution of estimates of other asteroid radar albedos. If we adopt a lower bound of 1.1 km on the effective diameter of 1991 CS, which is suggested by the hulls obtained on August 28 and 29, then the radar cross section and absolute magnitude of 1991 CS correspond to upper limits on the radar and optical geometric albedos of 0.25 and 0.14, respectively, that are consistent with its S-class taxonomy.

DISCUSSION

How unusual is the modest elongation of 1991 CS among the near-Earth asteroids? As noted above, the elongation of 1991 CS is the least of any NEA for which comparable information from radar observations is available, but that sample (8) is not large enough to determine whether the elongation is exceptional. Near-Earth asteroids are thought to be collisionally

evolved objects (Davis *et al.* 1989), thus information from hypervelocity impact cratering experiments and scaling laws may elucidate the expected abundance of elongations comparable to that of 1991 CS. Fragments produced in the experiments have mean elongations close to ~1.4 for a wide range of non-icy compositions and laboratory conditions (Fujiwara *et al.* 1989), suggesting that the elongation of 1991 CS is not unusual if the asteroid is a collisional fragment, under the assumption that laboratory-scale experiments can be extrapolated to kilometer-sized objects (Housen and Holsapple 1990). Constraints on the distribution of NEA elongations from convex hulls and three-dimensional shape reconstructions will grow significantly over the next decade now that the Arecibo upgrade is complete.

Table VIII lists future radar opportunies for 1991 CS in the interval 1998-2050 in which the estimated SNR per day exceeds 10. 1991 CS will next be detectable with existing radar systems in 2015. The next opportunity at least as good as the one in 1996 will occur in 2040 and could yield a detailed three-dimensional shape model.

ACKNOWLEDGMENTS

L. A. M. Benner was supported as a Research Associate of the National Research Council. Part of this research was conducted at the Jet Propulsion Laboratory, California Institute of Technology, under contract with NASA.

REFERENCES

Benner, L. A. M., S. J. Ostro, J. D. Giorgini, R. F. Jurgens, D. L. Mitchell, R. Rose, K. D. Rosema, M. A. Slade, R. Winkler, D. K. Yeomans, D. B. Campbell, J. F. Chandler, and I. I. Shapiro 1997. Radar detection of near-Earth asteroids 2062 Aten, 2101 Adonis, 3103 Eger, 4544 Xanthus, and 1992 QN. *Icarus* **130**, 296-312.

Benner, L. A. M., R. S. Hudson, S. J. Ostro, K. D. Rosema, J. D. Giorgini, D. K. Yeomans, R. F. Jurgens, D. L. Mitchell, R. Winkler, R. Rose, M. A. Slade, and M. L. Thomas 1998. Radar observations of asteroid 2063 Bacchus. Submitted to *Icarus*.

Chamberlin, A. B., D. K. Yeomans, P. W. Chodas, J. D. Giorgini, R. A. Jacobson, M. S. Keesey, J. H. Leiske, S. J. Ostro, E. M. Standish, and R. N. Wimberly 1997. JPL Solar system dynamics WWW site. *Bull. Am. Astron. Soc.* **29**, 1014 [Abstract]

Chapman, C. R., A. W. Harris, and R. Binzel 1994. Physical properties of near-Earth asteroids: Implications for the hazard issue. In *Hazards Due to Comets and Asteroids*, (T. Gehrels, Ed.), pp. 537-549. University of Arizona Press, Tucson.

Davis, D. R., S. J. Weidenschilling, P. Farinella, P. Paolicchi, and R. P. Binzel 1989. Asteroid collisional history: Effects on sizes and spins. In *Asteroids II* (R. P. Binzel, T. Gehrels, and M. S. Matthews, Eds.), pp. 805-826. University of Arizona Press, Tucson.

Fujiwara, A., P. Cerroni, D. Davis, E. Ryan, M. Di Martino, K. Holsapple, and K. Housen 1989. Experiments and scaling laws for catastrophic collisions. In *Asteroids II* (R. P. Binzel, T. Gehrels, and M. S. Matthews, Eds.), pp. 240-265. University of Arizona Press, Tucson.

Housen, K. R., and K. A. Holsapple 1990. On the fragmentation of asteroids and planetary satellites. *Icarus* **84**, 226-253.

Hudson, S. 1993. Three-dimensional reconstruction of asteroids from radar observations.

Remote Sensing Rev. **8**, 195-203.

Hudson, R. S., and S. J. Ostro 1994. Shape of asteroid 4769 Castalia (1989 PB) from inversion of radar images. *Science* **263**, 940-943.

Kendall, M., and A. Stuart 1979. *The Advanced Theory of Statistics. Volume 2. Inference and Relationship*. MacMillan, New York.

Love, S. G., and T. J. Ahrens 1997. Origin of asteroid rotation rates in catastrophic impacts. *Nature* **386**, 154-156.

Marsden, B. G. 1997. *Minor Planet Circ.* No. 30437.

McNaught, R. H., and K. S. Russell 1991. *IAU Circ.* 5190.

Mitchell, D. L., S. J. Ostro, K. D. Rosema, R. S. Hudson, D. B. Campbell, J. F. Chandler, and I. I. Shapiro 1995. Radar observations of asteroids 7 Iris, 9 Metis, 12 Victoria, 216 Kleopatra, and 654 Zelinda. *Icarus* **118**, 105-131.

Mitchell, D. L., R. S. Hudson, S. J. Ostro, and K. D. Rosema 1998. Shape of asteroid 433 Eros from inversion of Goldstone radar Doppler spectra. *Icarus* **131**, 4-14.

Ostro, S. J. 1993. Planetary radar astronomy. *Rev. Mod. Phys.* **65**, 1235-1279.

Ostro, S. J., D. B. Campbell, and I. I. Shapiro 1985. Mainbelt asteroids: Dual-polarization radar observations. *Science* **229**, 442-446.

Ostro, S. J., R. Connelly, and L. Belkora 1988. Asteroid shapes from radar echo spectra: A new theoretical approach. *Icarus* **73**, 15-24.

Ostro, S. J., K. D. Rosema, R. F. Jurgens 1990a. The shape of Eros. *Icarus* **84**, 334-351.

Ostro, S. J., D. B. Campbell, A. A. Hine, I. I. Shapiro, J. F. Chandler, C. L. Werner, and K. D. Rosema 1990b. Radar images of asteroid 1627 Ivar. *Astron. J.* **99**, 2012-2018.

Ostro, S. J., J. F. Chandler, A. A. Hine, K. D. Rosema, I. I. Shapiro, and D. K. Yeomans 1990c.

Radar images of asteroid 1989 PB. *Science* **248**, 1523-1528.

Ostro, S. J., D. B. Campbell, J. F. Chandler, A. A. Hine, R. S. Hudson, K. D. Rosema, and I. I. Shapiro 1991a. Asteroid 1986 DA: Radar evidence for a metallic composition. *Science* **252**, 1399-1404.

Ostro, S. J., D. B. Campbell, J. F. Chandler, I. I. Shapiro, A. A. Hine, R. Velez, R. F. Jurgens, K. D. Rosema, R. Winkler, and D. K. Yeomans 1991b. Asteroid radar astrometry. *Astron. J.* **102**, 1490-1502.

Ostro, S. J., D. B. Campbell, R. A. Simpson, R. S. Hudson, J. F. Chandler, K. D. Rosema, I. I. Shapiro, E. M. Standish, R. Winkler, D. K. Yeomans, R. Velez, and R. M. Goldstein 1992. Europa, Ganymede, and Callisto: New radar results from Arecibo and Goldstone. *J. Geophys. Res.* **97**, 18,227-18,244.

Ostro, S. J., K. D. Rosema, R. S. Hudson, R. F. Jurgens, J. D. Giorgini, R. Winkler, D. K. Yeomans, D. Choate, R. Rose, M. A. Slade, S. D. Howard, and D. L. Mitchell 1995. Extreme elongation of asteroid 1620 Geographos from radar images. *Nature* **375**, 474-477.

Ostro, S. J., R. F. Jurgens, K. D. Rosema, R. S. Hudson, J. D. Giorgini, R. Winkler, D. K. Yeomans, D. Choate, R. Rose, M. A. Slade, S. D. Howard, D. J. Scheeres, and D. L. Mitchell 1996. Radar observations of asteroid 1620 Geographos. *Icarus* **121**, 46-66.

Ostro, S. J., R. S. Hudson, K. D. Rosema, J. D. Giorgini, R. F. Jurgens, D. K. Yeomans, P. W. Chodas, R. Winkler, R. Rose, D. Choate, R. A. Cormier, D. Kelley, R. Littlefair, and M. A. Slade 1998. Asteroid 4179 Toutatis: 1996 radar observations. Submitted to *Icarus*.

Pravec, P., M. Wolf, and L. Sarounova 1998. Lightcurves of 26 near-Earth asteroids. Submitted to *Icarus*.

Tedesco, E. F. 1989. Asteroid magnitudes, UBV colors, and IRAS albedos and diameters. In

Asteroids II (R. P. Binzel, T. Gehrels, and M. S. Matthews, Eds.), pp. 1090-1138. University of Arizona Press, Tucson.

Thomas, P. C., R. P. Binzel, M. J. Gaffey, A. D. Storrs, E. N. Wells, and B. H. Zellner 1997. Impact excavation on asteroid 4 Vesta: Hubble Space Telescope results. *Science* **277**, 1492-1495.

Zellner, B. 1979. Asteroid taxonomy and the distribution of the compositional types. In *Asteroids* (T. Gehrels, Ed.), pp. 783-806. University of Arizona Press, Tucson.

TABLE I

Optically Determined Physical Properties

Property	Value
H (mag)	17.4[c], 17.5[d]
Class	S[a, b]
P (h)	2.390[d]
Δm	0.27 - 0.32[d]

Note. H is the absolute visual magnitude, class refers to the taxonomic class, P is the synodic rotation period in hours, and Δm indicates the range of observed lightcurve amplitudes.

[a] R. P. Binzel, personal communication.

[b] M. D. Hicks, personal communication.

[c] Marsden (1997)

[d] Pravec *et al.* (1998).

TABLE II

Observations

Date	RA (°)	DEC (°)	Distance (AU)	POS motion (°)	P_{TX} (kW)	Runs	Δt (UTC hours)	Rotations	Δf (Hz)
1996 August 26	36.35	20.27	0.057	2.6	485	100	11.37 - 17.10	2.40	0.98
1996 August 27	41.20	10.34	0.053	3.5	487	161	10.49 - 16.93	2.69	0.98
1996 August 28	46.51	-0.90	0.051	2.6	485	101	09.90 - 15.01	2.14	0.98
1996 August 29	51.99	-12.46	0.051	2.6	485	129	10.13 - 15.50	2.24	0.98

Note. Right ascension, declination, and distance are given at the middle of each day's observations. Plane-of-sky (POS) motion between start of reception of the first echo and end of reception of the last echo on each day is indicated. Total POS motion between the beginning of the experiment on August 26 and the end on August 29 was ~39°. P_{TX} is the average transmitter power. The number of transmit-receive cycles (runs) is listed in the sixth column. Δt is the interval spanned by observations. The number of rotations covered on each day is listed in the ninth column, where we have adopted the rotation period in Table I. Δf is the raw frequency resolution.

TABLE III

Disc-Integrated Radar Properties

Date	OC SNR	B (Hz)	$\sigma_{OC} \pm 35\%$ (km^2)	μ_C
1996 August 26	309	41	0.24	0.25 ± 0.003
1996 August 27	470	45	0.23	0.28 ± 0.002
1996 August 28	434	50	0.29	0.26 ± 0.002
1996 August 29	329	49	0.18	0.29 ± 0.003
whole experiment	771	50	0.24	0.28 ± 0.001

Note. Radar properties on each date, determined from weighted sums of cw spectra. OC SNR is the OC signal-to-noise ratio obtained from an optimally filtered weighted spectral sum. B is the maximum 2-sigma level bandwidth from weighted sums of spectra grouped into 30° rotation phase intervals, an approach adopted to avoid smear due to the target's slightly elongated shape. σ_{OC} is the OC radar cross section; assigned uncertainties are the root sum square of systematic calibration errors that are estimated to be $\leq 35\%$ of the radar cross section.

TABLE IV

Doppler Radar Astrometry

Date	UTC Epoch	OSOD Solution	Correction	Measurement	Uncertainty
1996 August 26	14:10:00	3	-4.5 Hz	491,117.6 Hz	0.5 Hz
1996 August 27	13:30:00	3	-6.3 Hz	299,050.4 Hz	0.4 Hz
1996 August 28	12:30:00	3	-8.3 Hz	77,608.1 Hz	0.8 Hz
1996 August 29	12:40:00	3	-8.9 Hz	-171,558.3 Hz	0.7 Hz

Note. Radar astrometry for echoes from 1991 CS' estimated center of mass, received at the stated UTC epoch. The reference point for the Goldstone antenna (DSS-14) is the intersection of the elevation and azimuth axes.

TABLE V

1991 CS Orbit (OSOD-6)

Epoch (TDB)	1997 December 18.0
Eccentricity, e	0.1645497508 (888)
Perihelion distance, q (AU)	0.938020843 (105)
Perihelion Passage (TDB)	1998 Jan 7.0405865 (388)
Argument of perihelion, ω (°)	249.4035180 (363)
Longitude of ascending node, Ω (°)	156.91746182 (617)
Inclination, i (°)	37.1227318 (460)

Note. These orbital elements are from a fit to optical and radar observations over the interval 1991 January 19 to 1997 July 29. A total of 200 optical astrometric observations are included. The radar data include four Doppler estimates in Table IV. We used JPL ephemeris DE-405 (J2000). The rms residual for all 200 optical observations is 0.92 arc sec and the radar rms residual is 0.14 Hz. The angular orbital elements are referred to the ecliptic and mean equinox of J2000 and 3-sigma standard errors (in parentheses) are given in units of the last decimal place.

TABLE VI

Constraints on Pole-on Dimensions

Date	Maximum bandwidth D_{max} (km/cosδ)	Phase (°)	Minimum bandwidth D_{min} (km/cosδ)	Phase (°)	D_{max}/D_{min}
Aug 26	1.01	134	0.88	216	1.16
Aug 27	1.17	108	0.97	31	1.20
Aug 28	1.28	120	1.09	22	1.18
Aug 29	1.31	125	1.09	171	1.20

Note. Lower bounds on maximum and minimum pole-on dimensions from convex hulls on each day. Rotation phases relative to a zero-phase epoch of 1996 August 26 11:21:57 UTC for the extrema are given in columns three and five.

TABLE VII

Near-Earth asteroid elongations

Asteroid	Pole-on elongation	Reference
433 Eros	2.2	Mitchell *et al.* 1998
1620 Geographos	2.8	Ostro *et al.* 1995, 1996
1627 Ivar	2.1	Ostro *et al.* 1990b
2063 Bacchus	2.1	Benner *et al.* 1998
4179 Toutatis	2.4	Hudson and Ostro 1995
4769 Castalia	1.6	Hudson and Ostro 1994
6178 1986 DA	1.4	Ostro *et al.* 1991a
7822 1991 CS	1.2	

Note: Pole-on elongations estimated from convex hulls or three-dimensional shape reconstructions. For the non-principal axis rotator Toutatis, we list the ratio of the long to the intermediate axis from its shape model.

TABLE VIII

7822 (1991 CS) Radar Opportunities: 1998-2050

Date	Distance (AU)	Arecibo SNR	Goldstone SNR
2015	0.165	160	10
2016	0.181	120	
2021	0.156	220	10
2022	0.279	20	
2040	0.074	4600	300
2041	0.185	110	
2046	0.235	40	

Note. Predictions for future observations in which the OC SNR per day exceeds 10 for nominal telescope parameters.

FIGURE CAPTIONS

FIG. 1. Rotation phase coverage of the 1991 CS observations. Each cross denotes rotation phase coverage for the specified date based on a synodic rotation period $P = 2.390$ h (Pravec *et al.* 1998), where the arrow at 12 o'clock indicates zero phase, rotation phase increases clockwise, and the zero-phase epoch is set at the start of reception of the our first echo at 1996 August 26 11:21:57 UTC. Radial line segments are proportional to the standard deviation of each spectrum. The first run on each day is indicated with a thick segment. Each concentric ring indicates successive rotations of the asteroid relative to the start of observations on that day.

FIG. 2. Echo power spectra from August 26, 27, 28, and 29 at the raw 0.98-Hz resolution. Echo power is plotted in standard deviations versus Doppler frequency relative to the estimated frequency of echoes from the asteroid's center of mass. Solid and dashed lines denote echo power in the OC and SC polarizations. Rotation phase coverage is indicated with inset crosses and radial line segments.

FIG. 3. Grayscale images of OC echo power spectra on each date. Pixels in each row show OC echo power from a single run in standard deviations versus Doppler frequency at the raw 0.98-Hz resolution. Time and rotation phase increase from top to bottom and are only approximately linear due to gaps in the data, which are shown with black rows. Pixels below a clipping level of 0 standard deviations are mapped to black and pixels above a saturation threshold of 24% are mapped to white.

FIG. 4. Evolution of echo power spectra on each date. Each spectrum is a weighted sum spanning 10° of rotation phase and has been filtered to a frequency resolution of 4 Hz. Labels give the weighted mean rotation phase in degrees. Each spectrum is centered on 0 Hz and extends from -50 Hz on the left to +50 Hz on the right. Identical linear scales are used throughout the figure. A vertical bar at 0 Hz indicates ± 1 standard deviation of the OC receiver noise.

FIG. 5. OC echo power spectra obtained on opposite sides of 1991 CS on August 27, 28 and 29 at rotation phases between 0 and 29° (thin solid curves) and between 180 and 209° (thin dashed curves). The weaker of each spectral pair was scaled to the peak SNR of the stronger spectrum to faciliate comparisions with their edge frequencies and shapes. Spectra obtained between 180 - 209° were subtracted from spectra obtained between 0 - 29°. The differenced spectra are shown with thick solid curves and shifts in the edge frequencies are noted with arrows. Rotation phase coverage is denoted with inset crosses.

FIG. 6. OC and SC radar cross sections plotted versus rotation phase for each day. Horizontal lines indicate the OC cross section from weighted sums of spectra listed in Table III.

FIG. 7. Estimates of μ_C plotted versus rotation phase for each day. Error bars denote ± 1-standard deviation errors. Horizontal lines indicate the value of μ_C from weighted sums of spectra listed in Table III.

FIG. 8. Ecliptic positions of 1991 CS during 1996 August 26 - 29. Lines depict the range of ecliptic motion during each day's observations and large dots indicate positions at the mid-point of

each day's observations.

FIG. 9. Convex hull and quantities associated with hull estimation for a) August 26, b) August 27, c) August 28, and d) August 29. Top) Estimate of the hull. "X" marks the projected position of asteroid's center of mass. Rotation phase convention follows that used in Fig. 1 and is indicated with an inset cross. Bottom) Open circles are support function data $\mathbf{p}_{\mathbf{dat}}$ as a function of rotation phase. Superimposed on $\mathbf{p}_{\mathbf{dat}}$ are solid and dashed curves (that are almost coincident) that correspond to the constrained Fourier model $\mathbf{p}_{\mathbf{con}}$ and the unconstrained Fourier model $\mathbf{p}_{\mathbf{unc}}$. The dashed curve at the top is the hull's bandwidth $p_{con}(\phi) + p_{con}(\phi+180°)$ and the solid curve at the bottom is the hull's middle frequency $[p_{con}(\phi) - p_{con}(\phi+180°)]/2$.

FIG. 10. Constraints on the diameter, radar albedo, and visual geometric albedo of 1991 CS. Radar albedo is shown as a thick solid curve that was computed using 1991 CS' radar cross section (Table III). Thin solid curves denote 1-sigma uncertainty in the radar albedo that propagates from uncertainty in σ_{OC}. The distribution by taxonomic class of main-belt and near-Earth asteroid radar albedos is superimposed on the radar albedo curve and is plotted solely as a function of radar albedo. Allowed geometric albedos (dash-dot curve) were computed as a function of diameter from $\log p_v = 6.244 - 2\log D - 0.4H$ (Zellner 1979), where H is 1991 CS' absolute magnitude (Table I). Mean and rms dispersions of the geometric albedos for the C, M, S, and E taxonomic classes (Tedesco 1989) are indicated by asterisks and adjacent thick curves. The geometric albedo of V-class asteroid 4 Vesta is shown with an asterisk (Tedesco 1989, Thomas *et al.* 1997). A vertical dashed line at $D_{max} = 1.1$ km denotes a lower bound on the minimum pole-on breadth from the August 28 and 29 convex hulls.

P = 2.390 hours

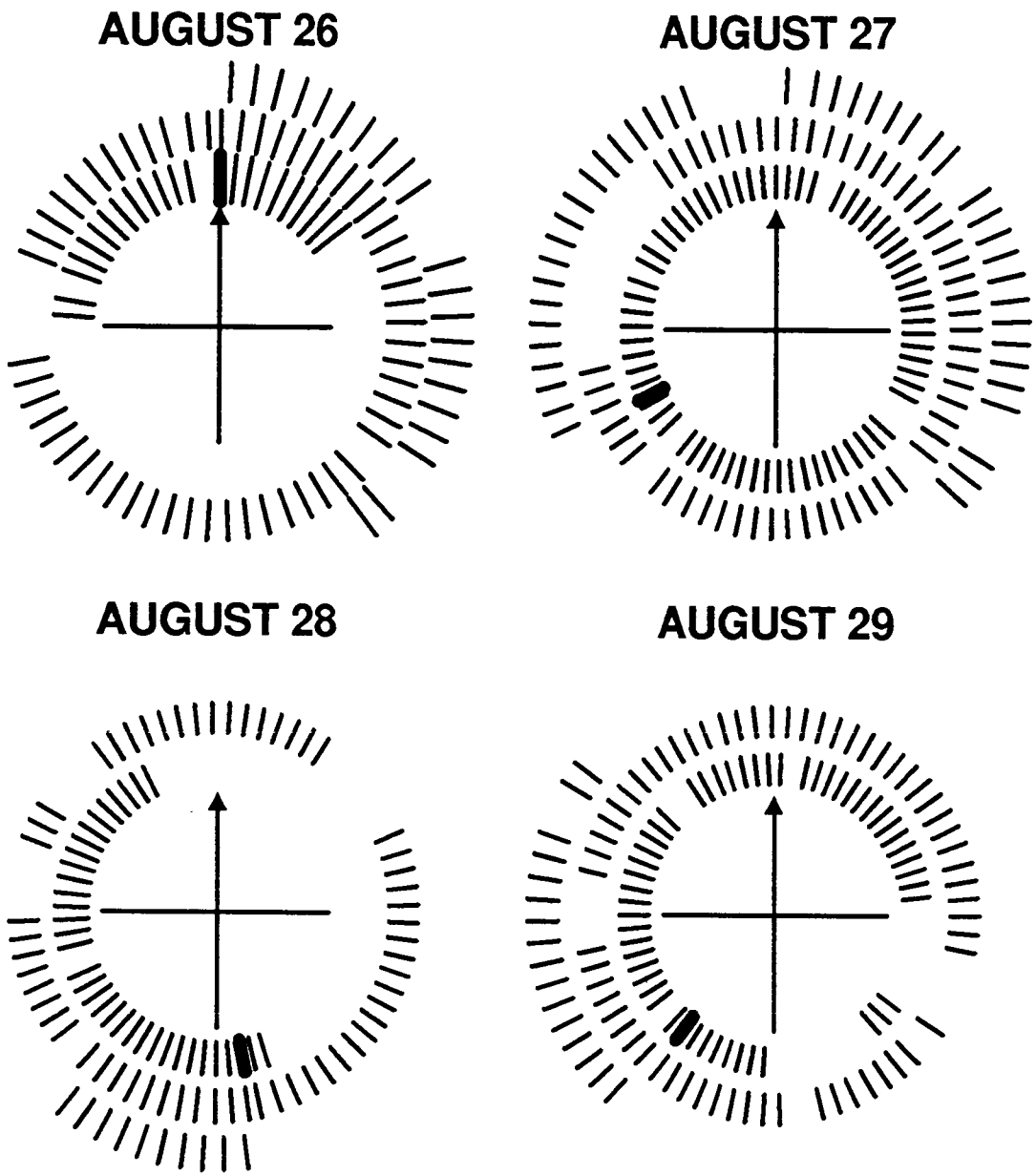

Zero-phase epoch: 1996 August 26 11:21:57 UTC

FIG. 1

2.18.98

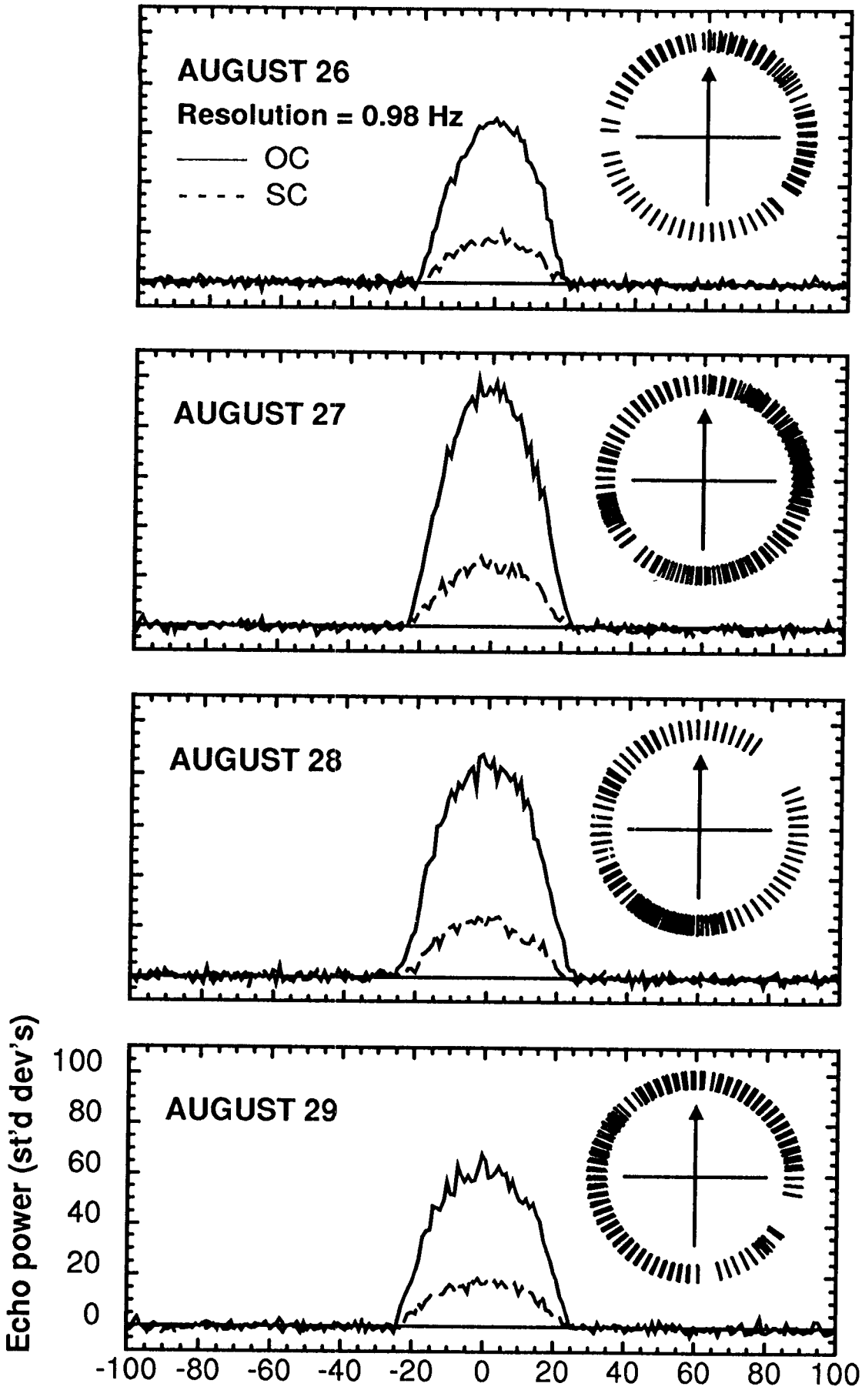

FIG. 2

cs.fig

AUGUST 26

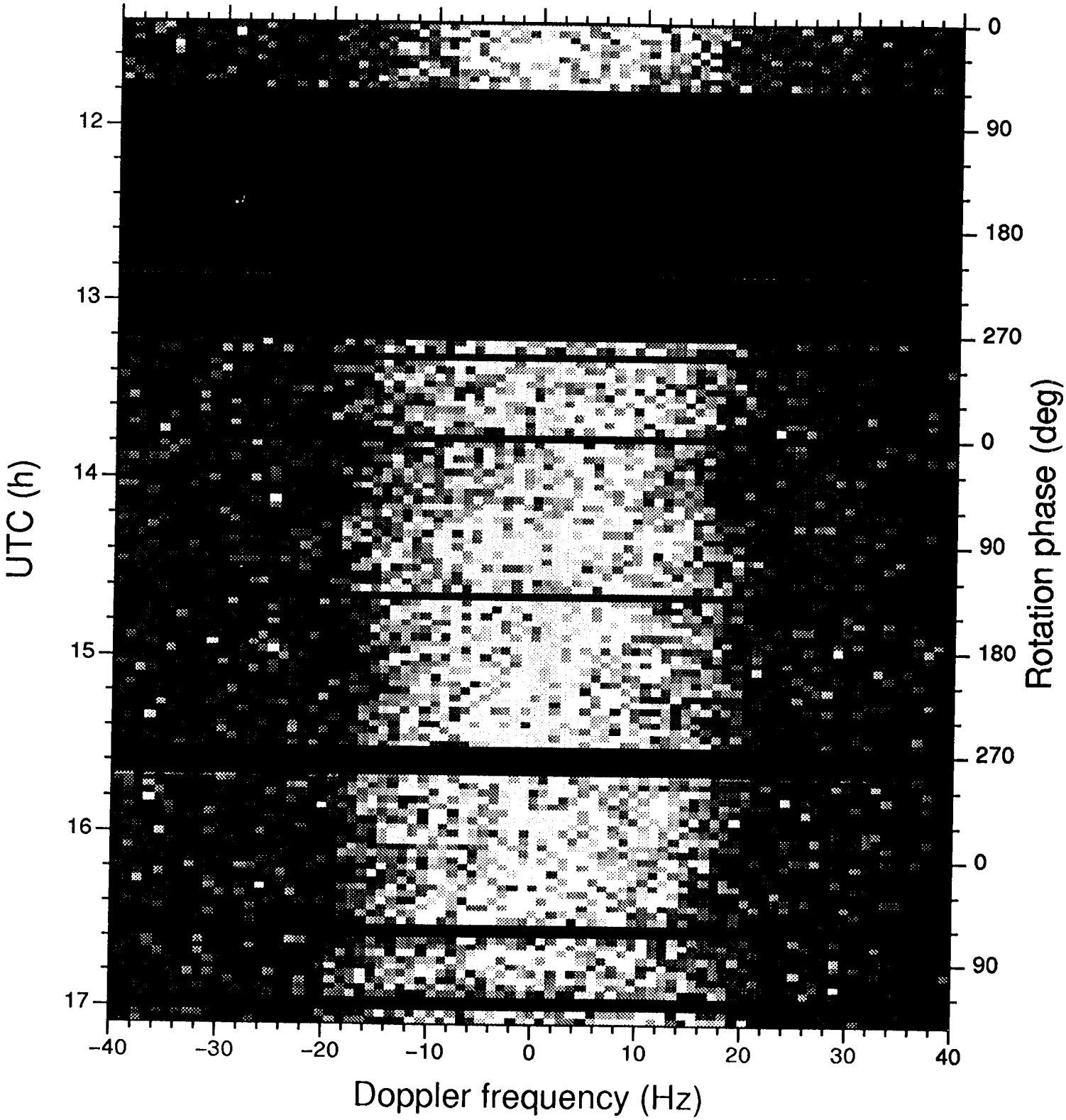

FIG. 3A

0239 image.tpl

6·22·98

AUGUST 27

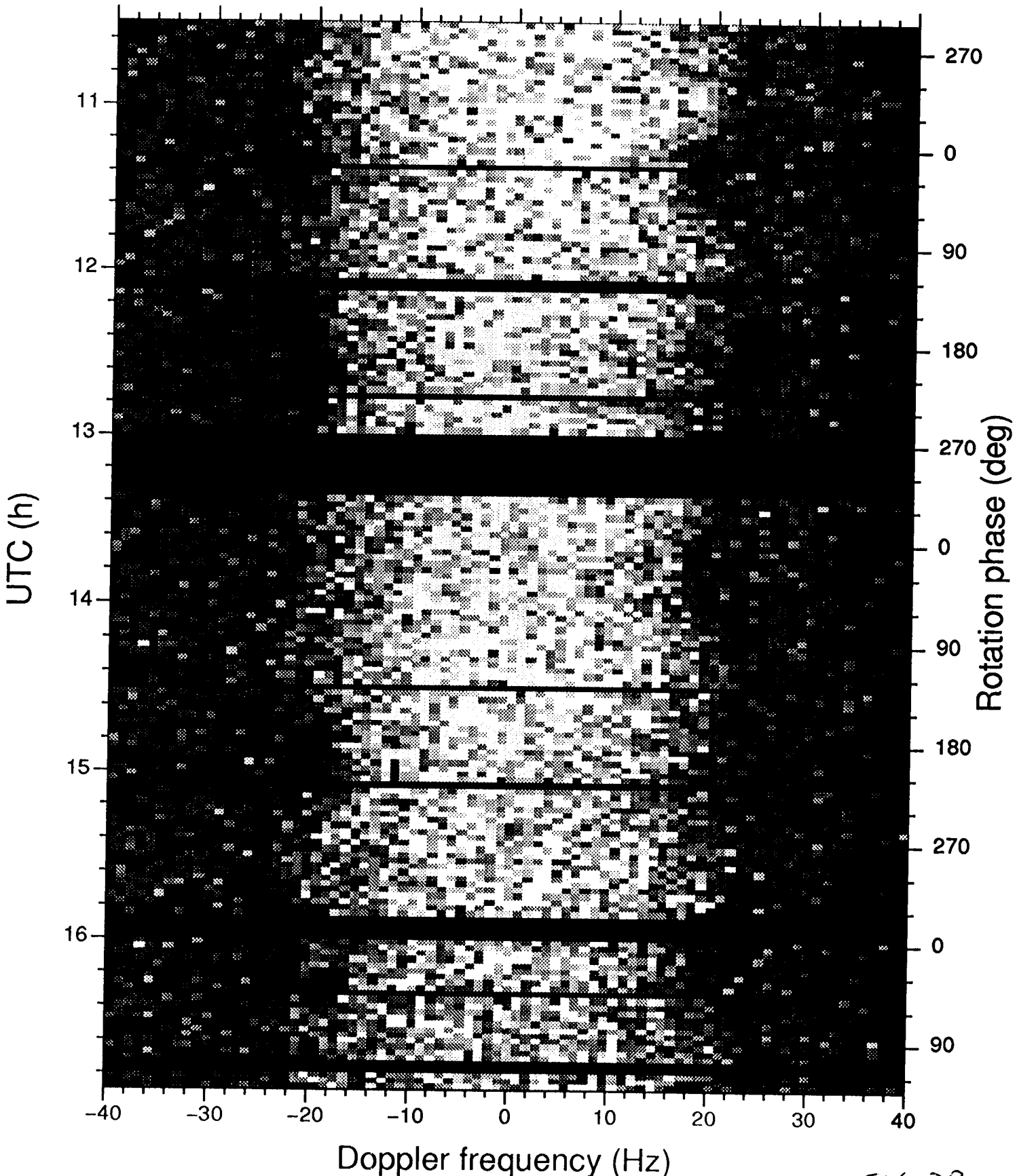

FIG. 3B

240 image.ppt

6.22.98

AUGUST 28

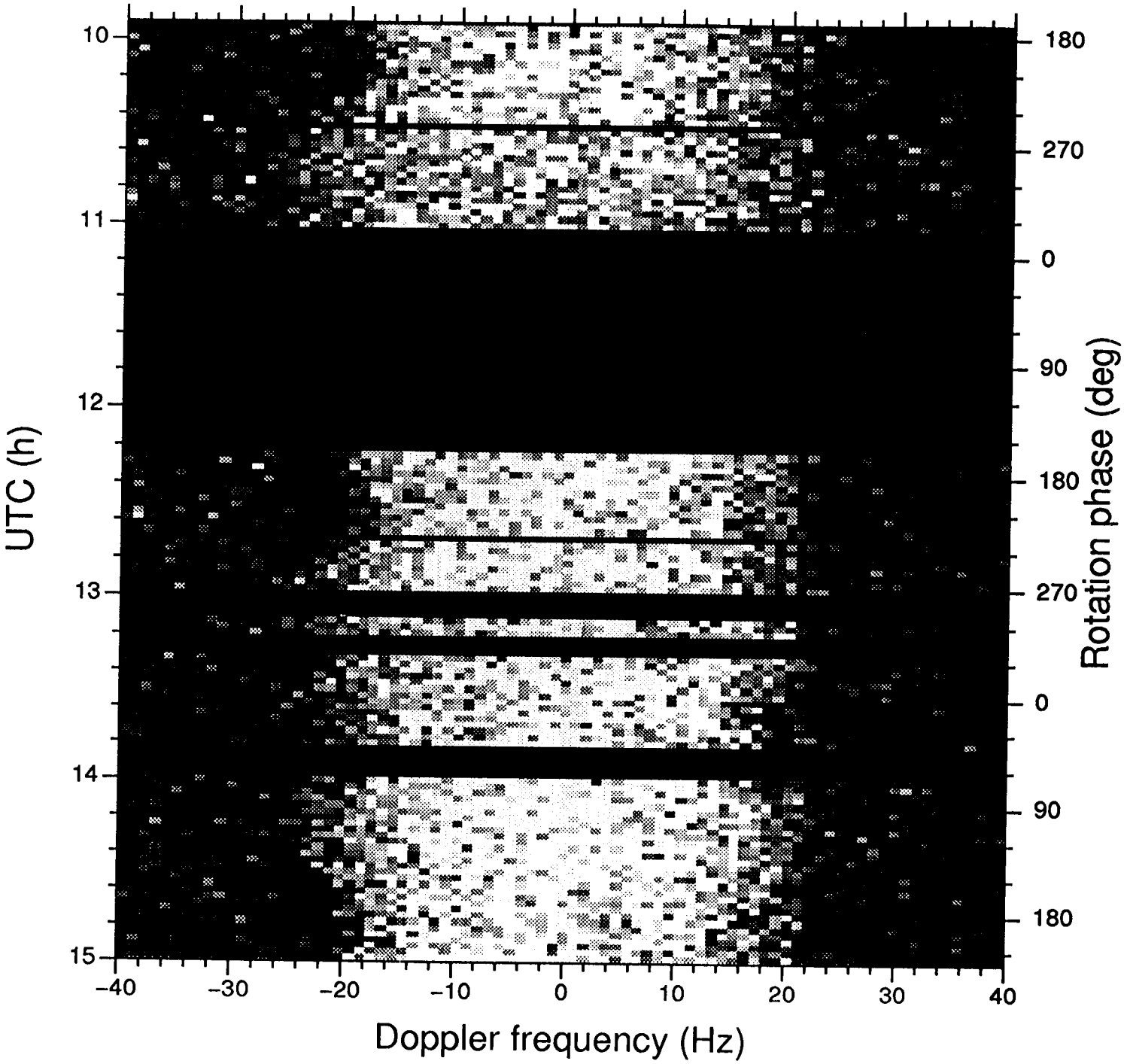

FIG. 3C

c:\24\image.tpl

6.22.98

AUGUST 29

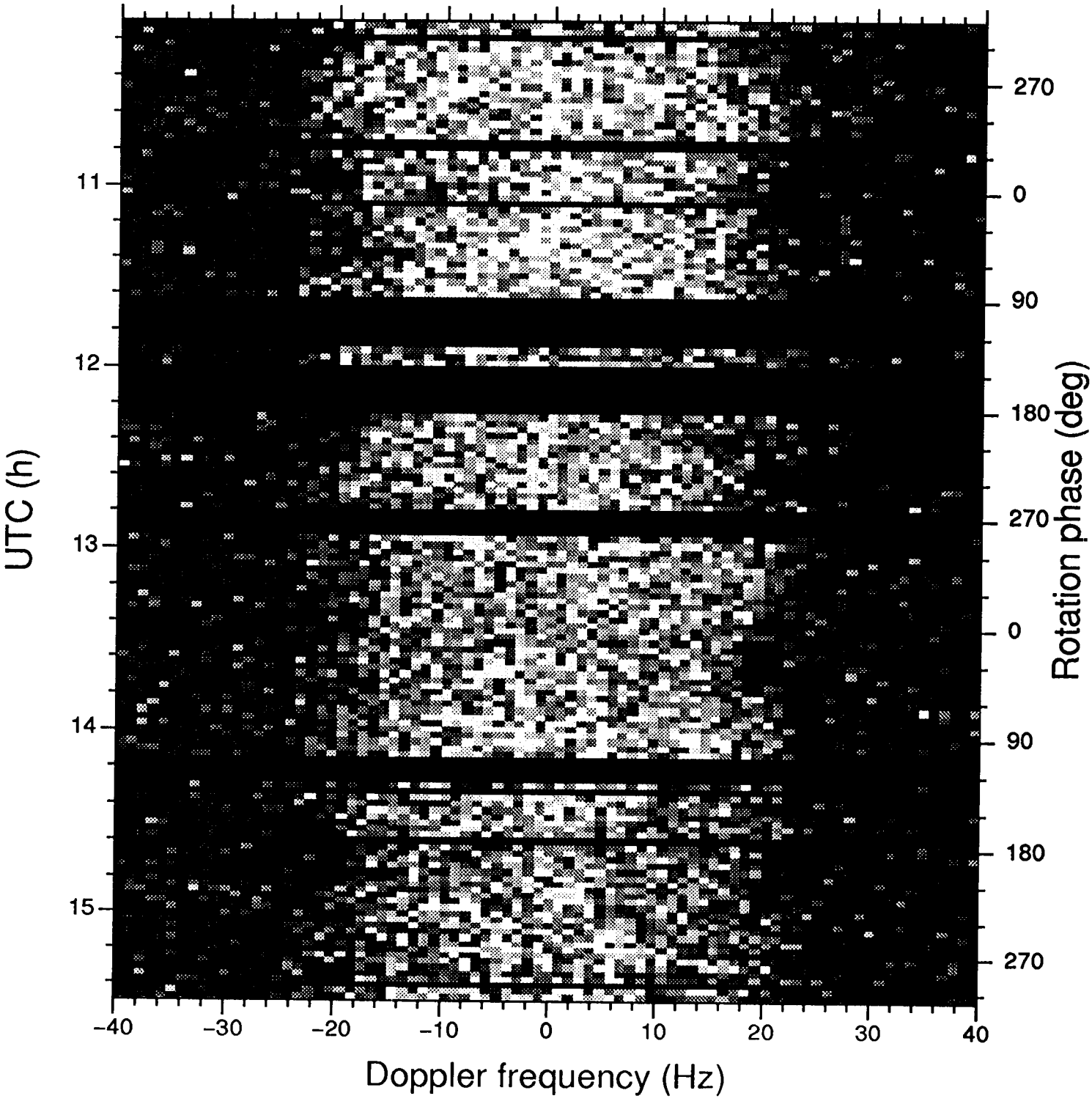

FIG. 3D

242image.tpl

6.18.98

AUGUST 26

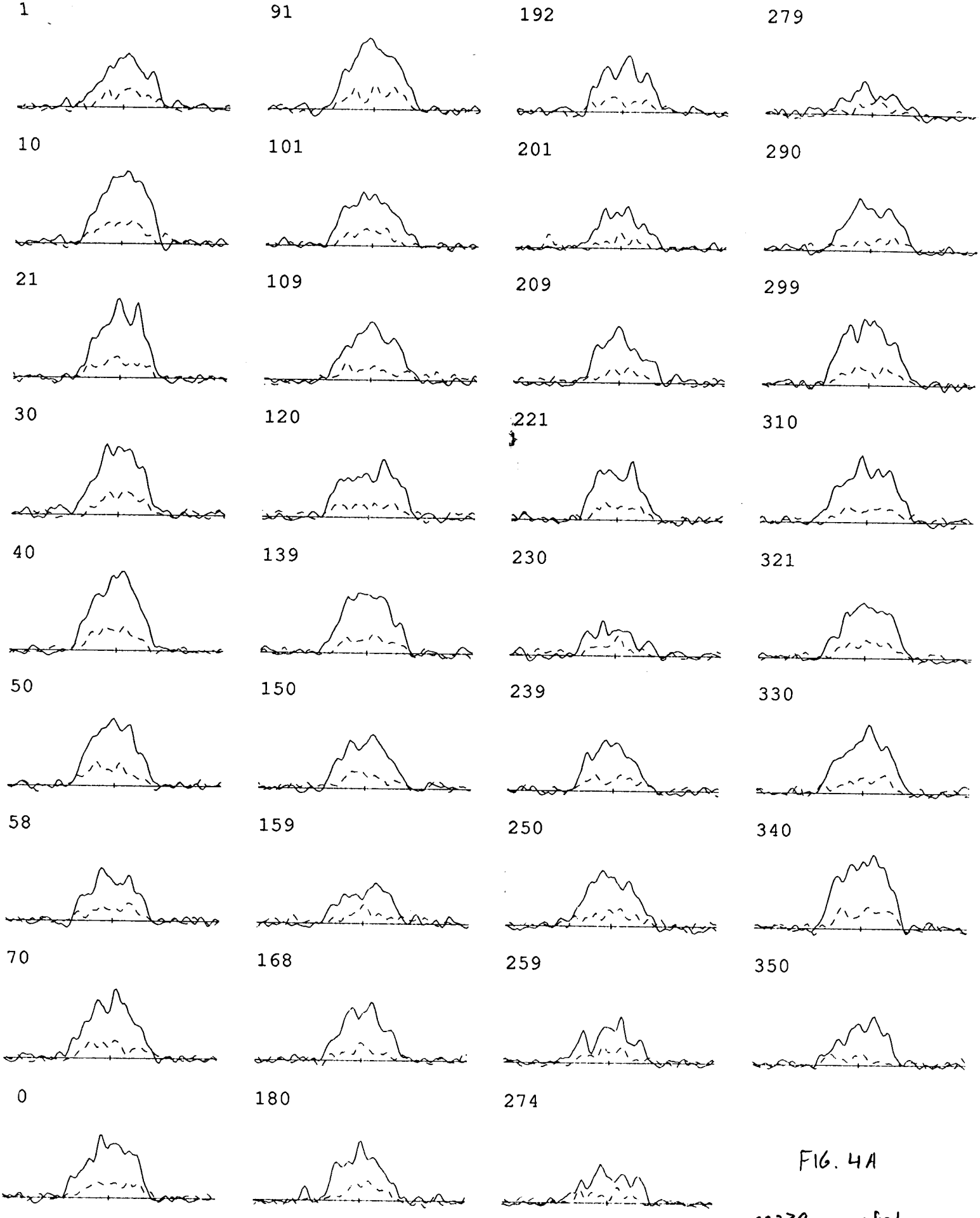

FIG. 4A

cs239.movie.fp1

6.18.98

AUGUST 27

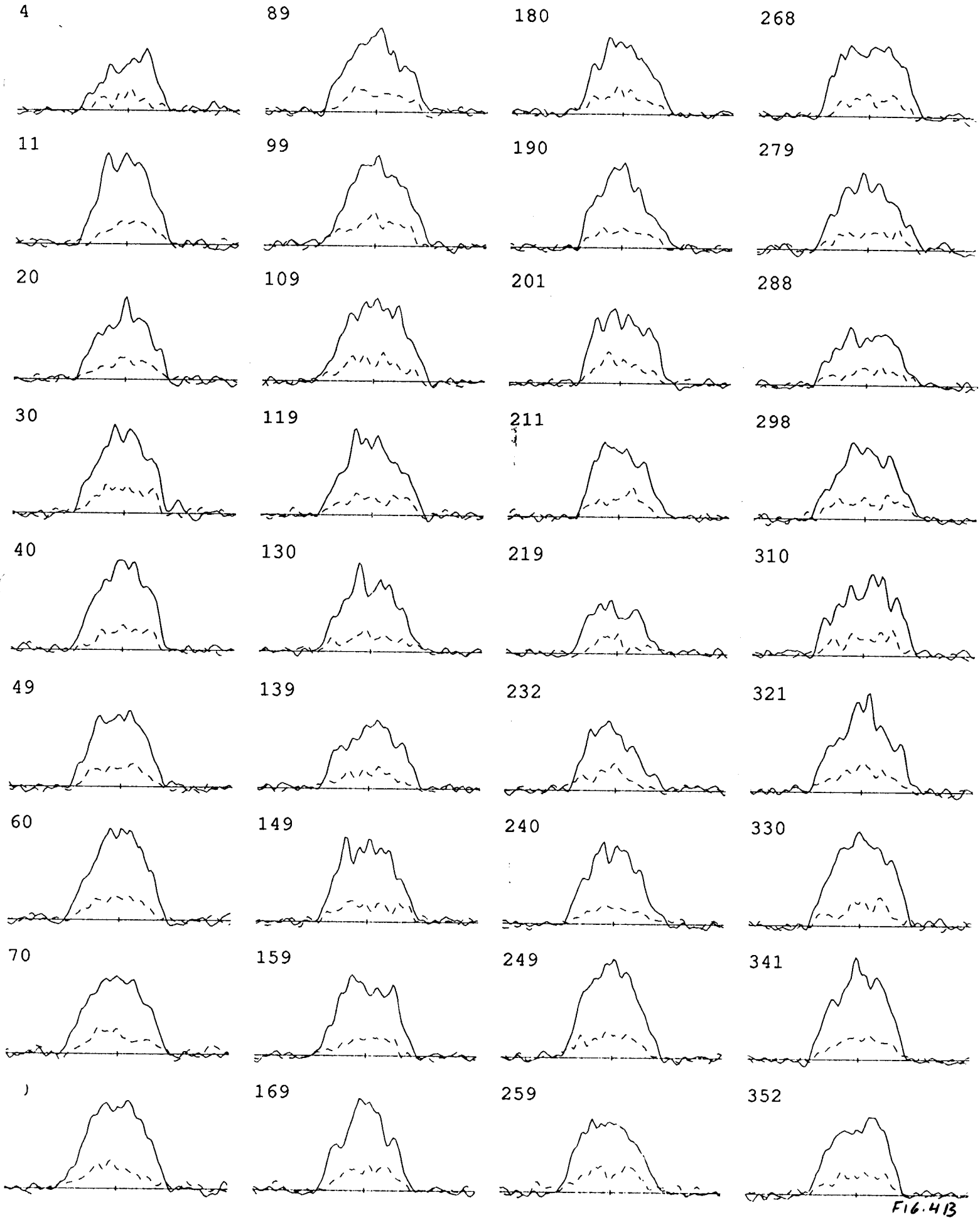

F16.413

cs240.movie.tp1

6.18.98

AUGUST 28

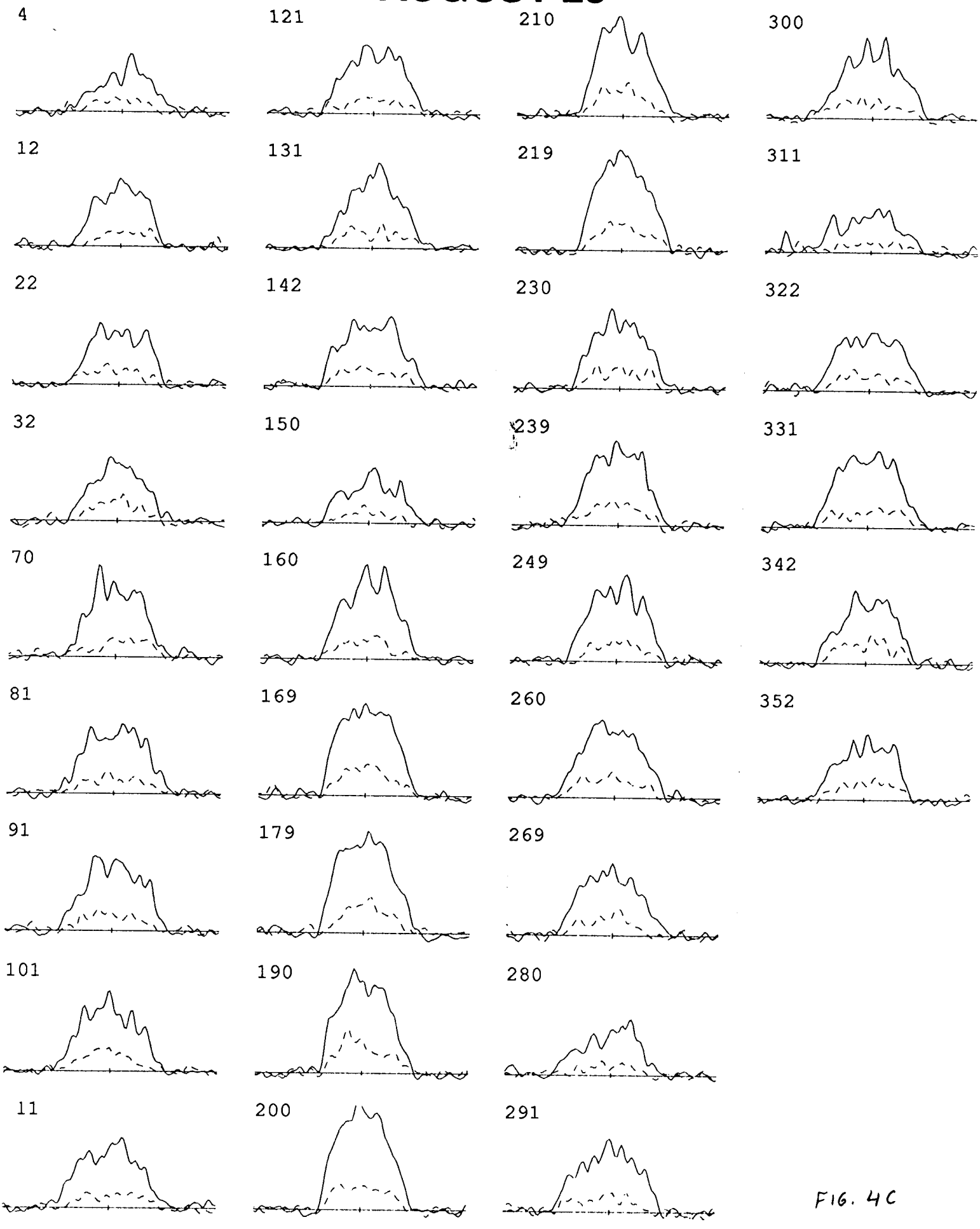

FIG. 4C

cs241.movie.tpl

6.18.98

AUGUST 29

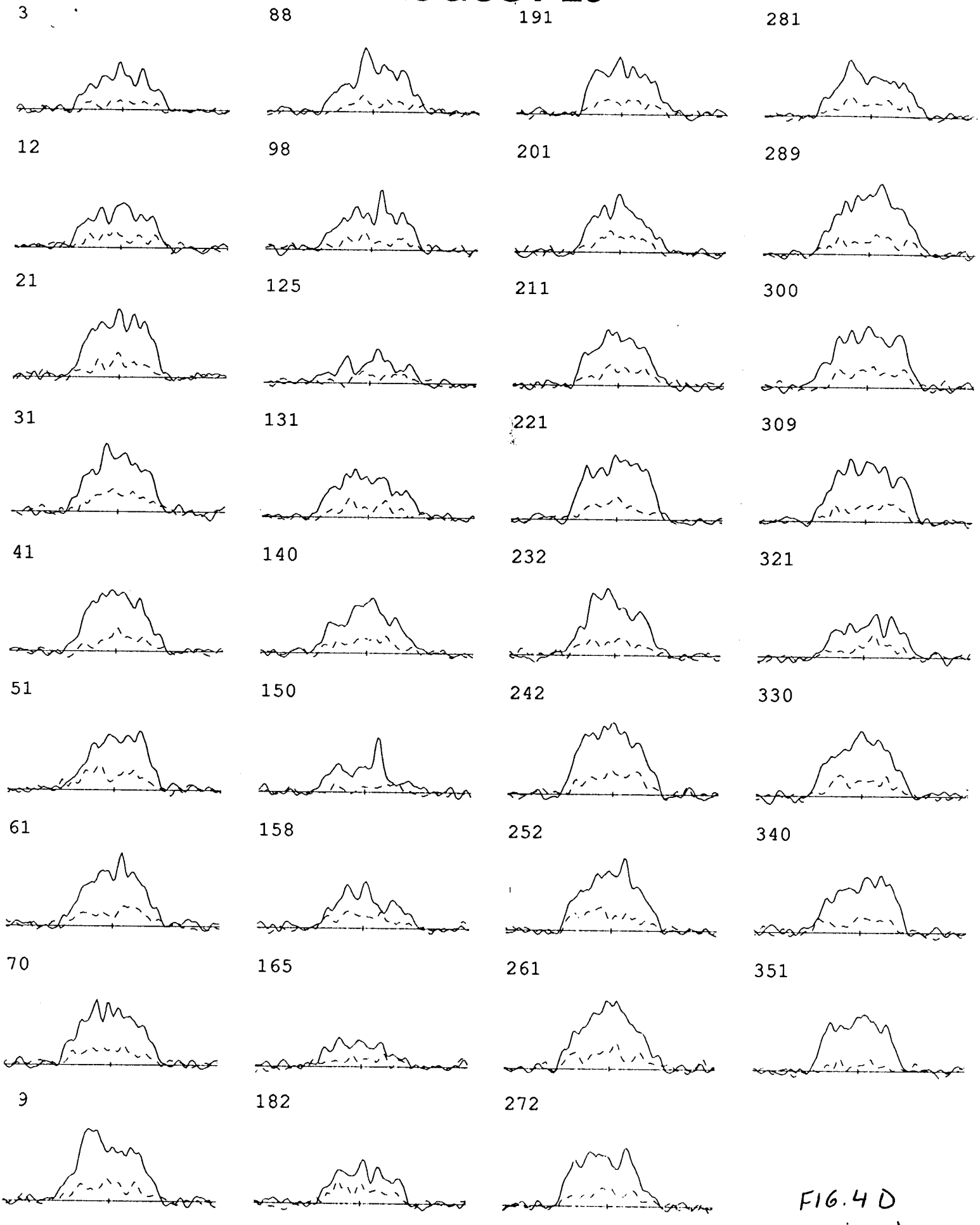

FIG. 4D

cs242.movie.mp1

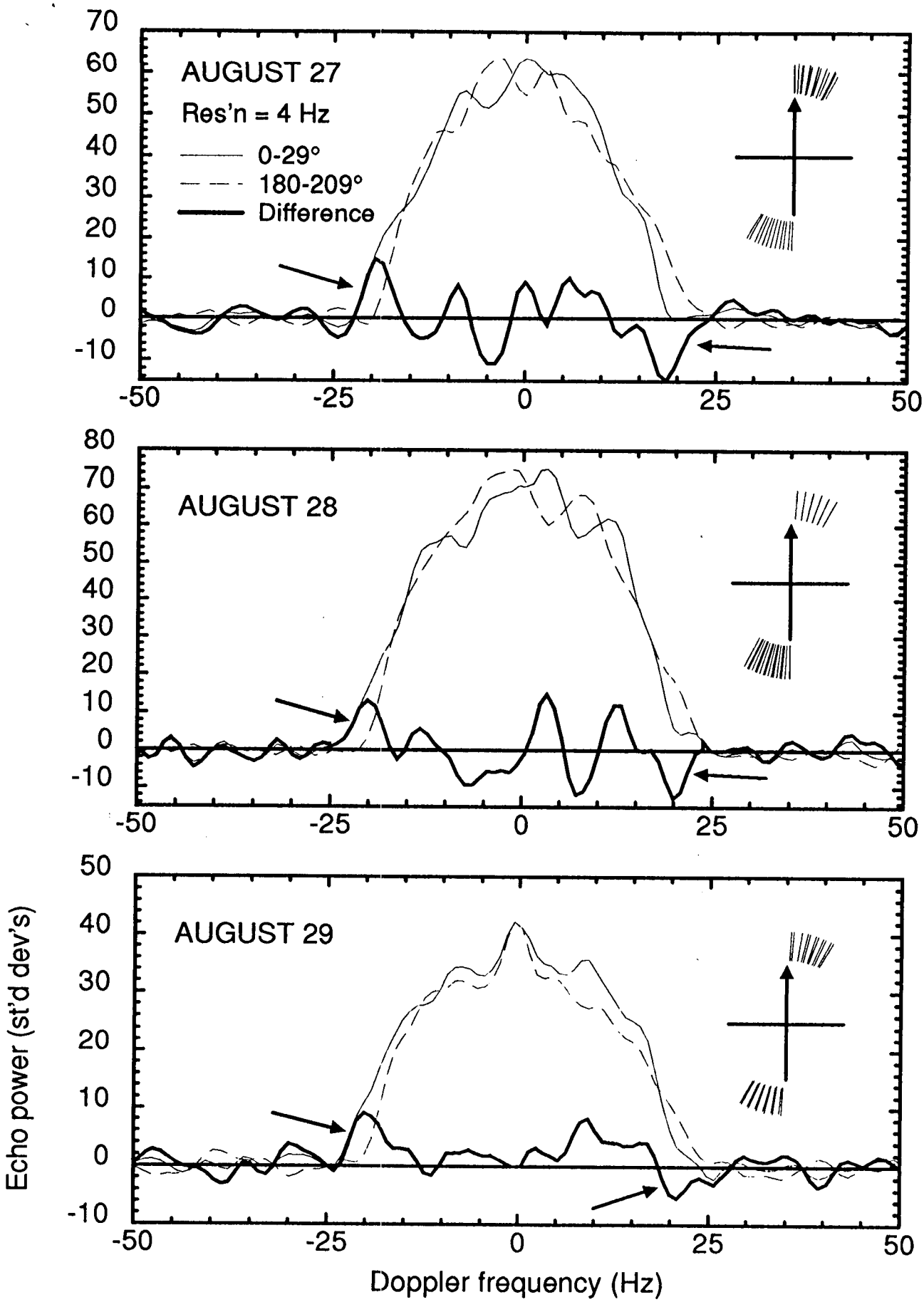

FIG. 5

cs.oppsides.fig

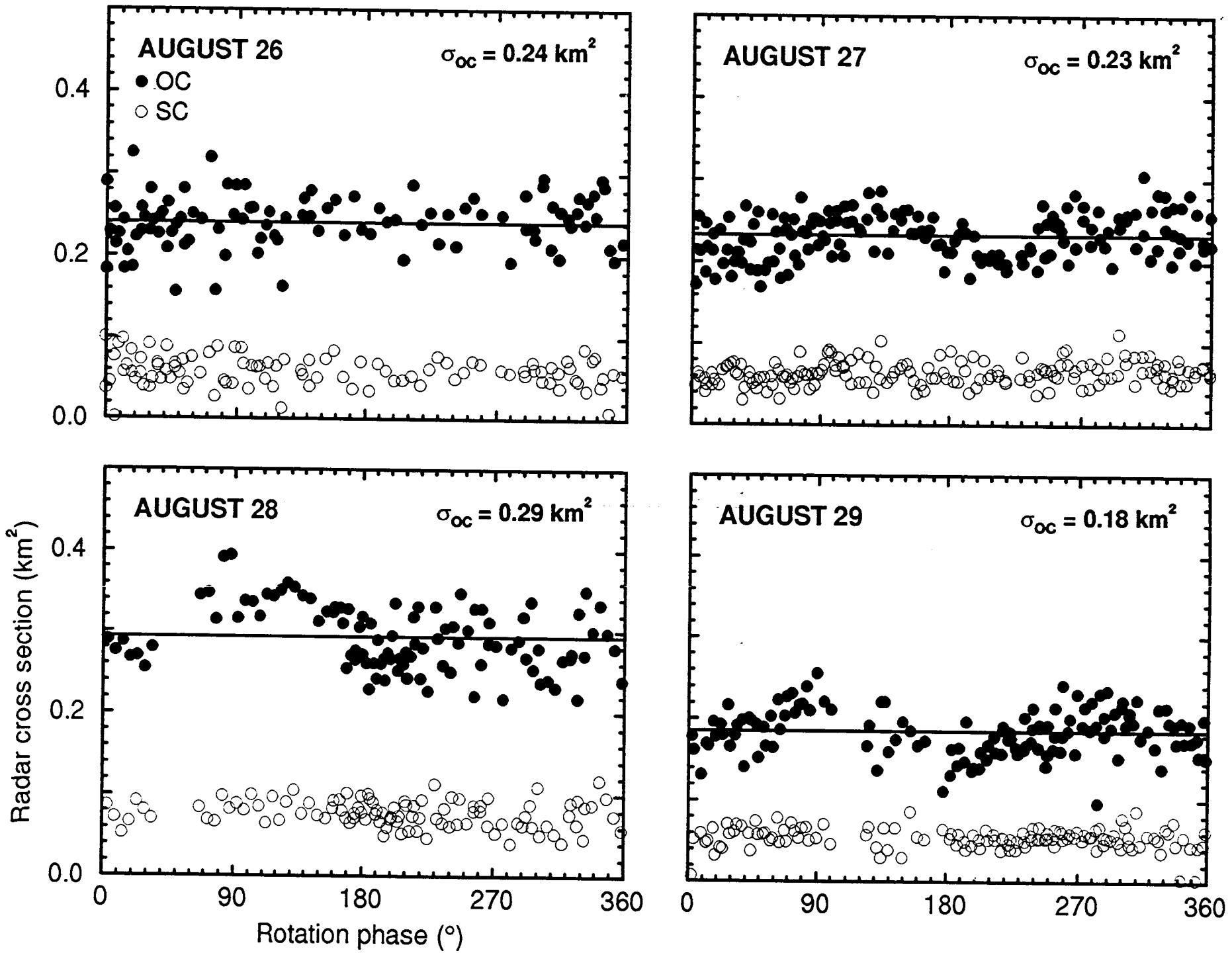
AUGUST 26
σ_{oc} = 0.24 km^2
OC
SC
AUGUST 27
σ_{oc} = 0.23 km^2
AUGUST 28
σ_{oc} = 0.29 km^2
AUGUST 29
σ_{oc} = 0.18 km^2
Radar cross section (km^2)
0.0
0.2
0.4
0
90
180
270
360
Rotation phase (°)

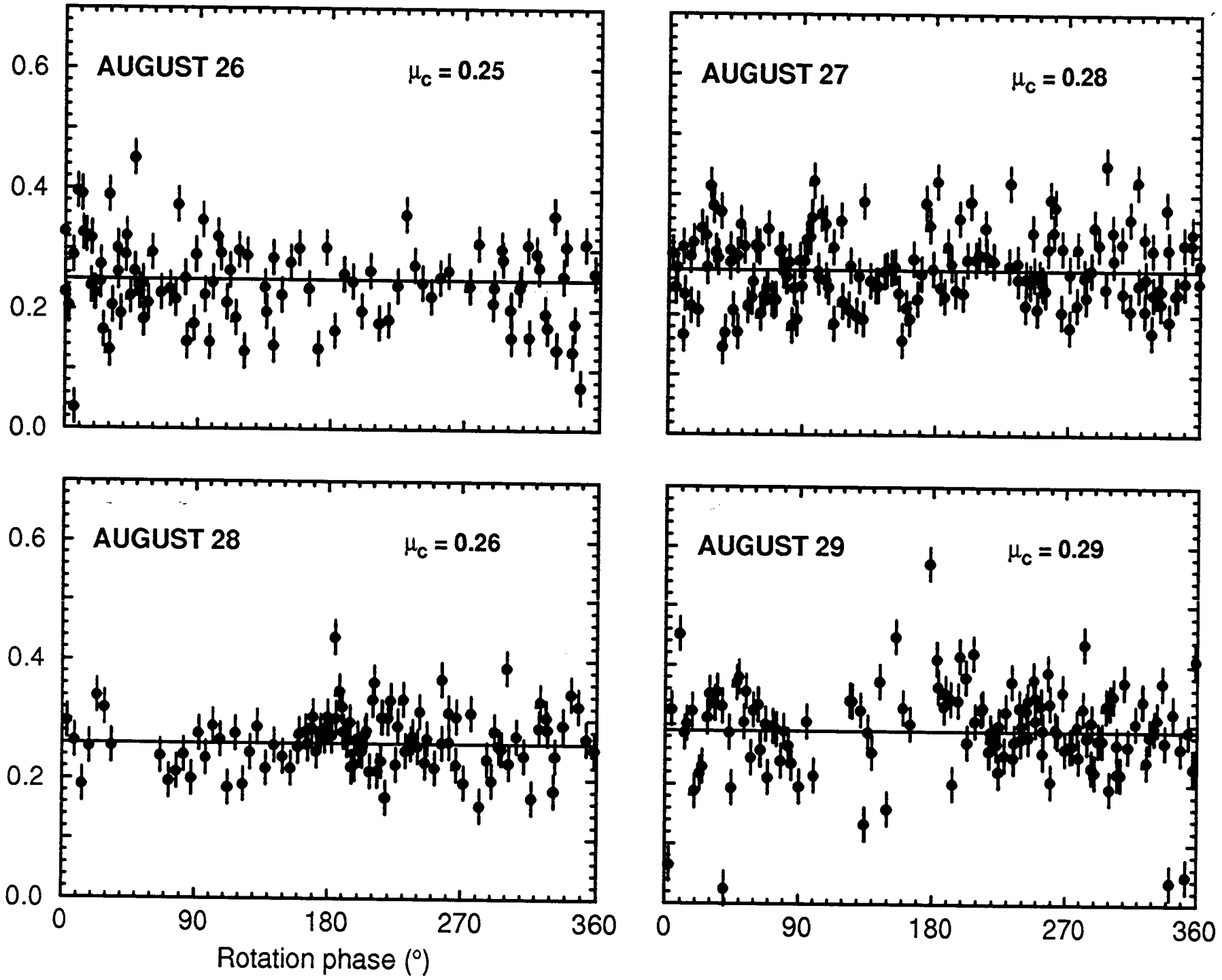

Fig. 7

Cramer, fig

6.17.98

10
0
-10
-20
-30
35
40
45
50
55
Ecliptic Latitude (°)
Ecliptic Longitude (°)
AUGUST 26
AUGUST 27
AUGUST 28
AUGUST 29

Fig. 8

6.17.98

AUGUST 26

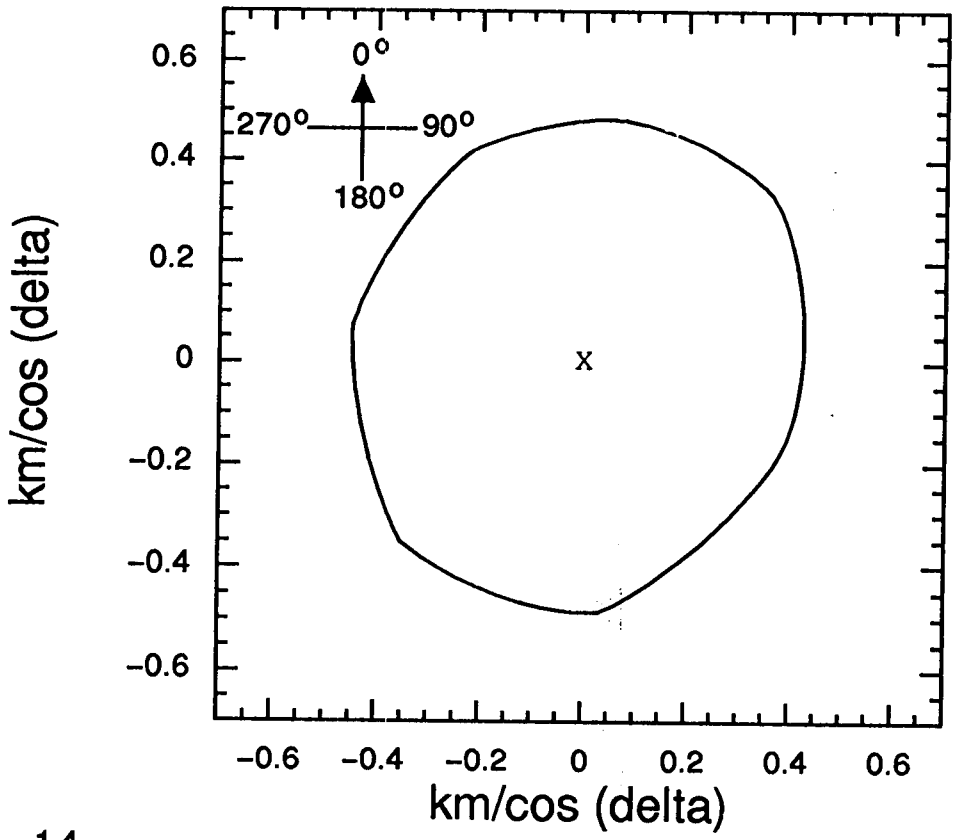

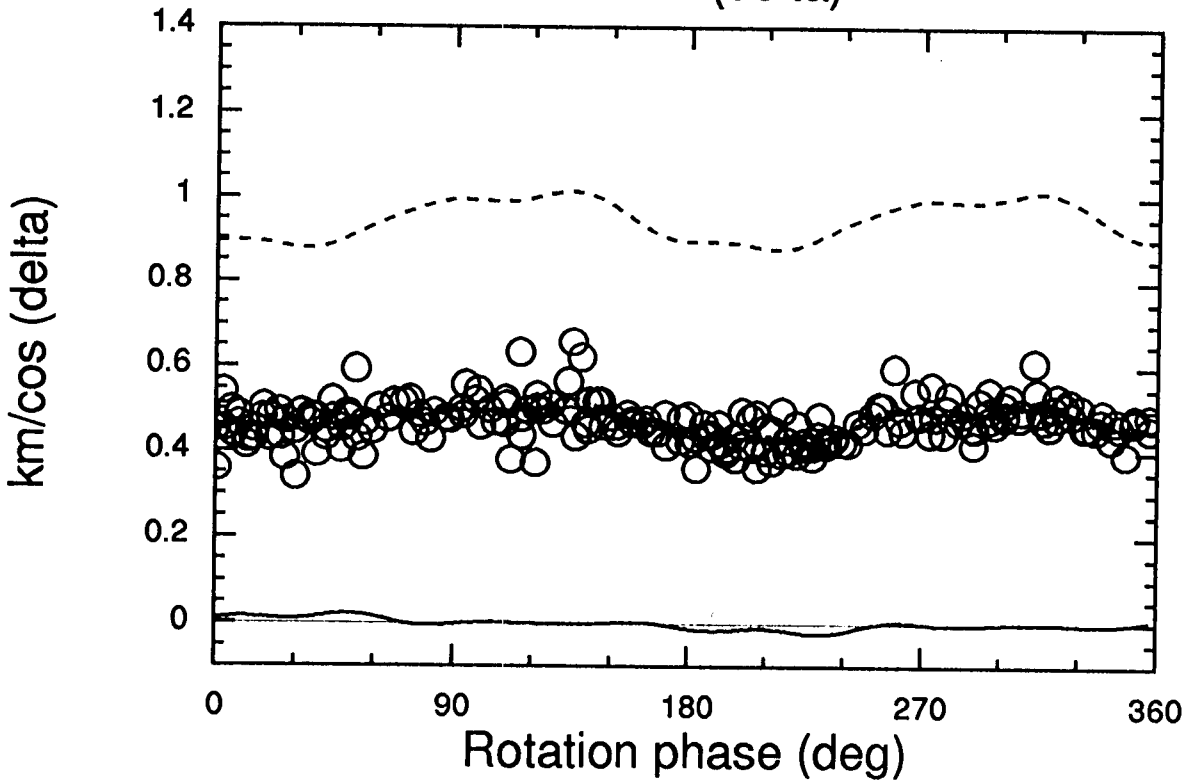

CS239hull.tpl

6.17.98

AUGUST 27

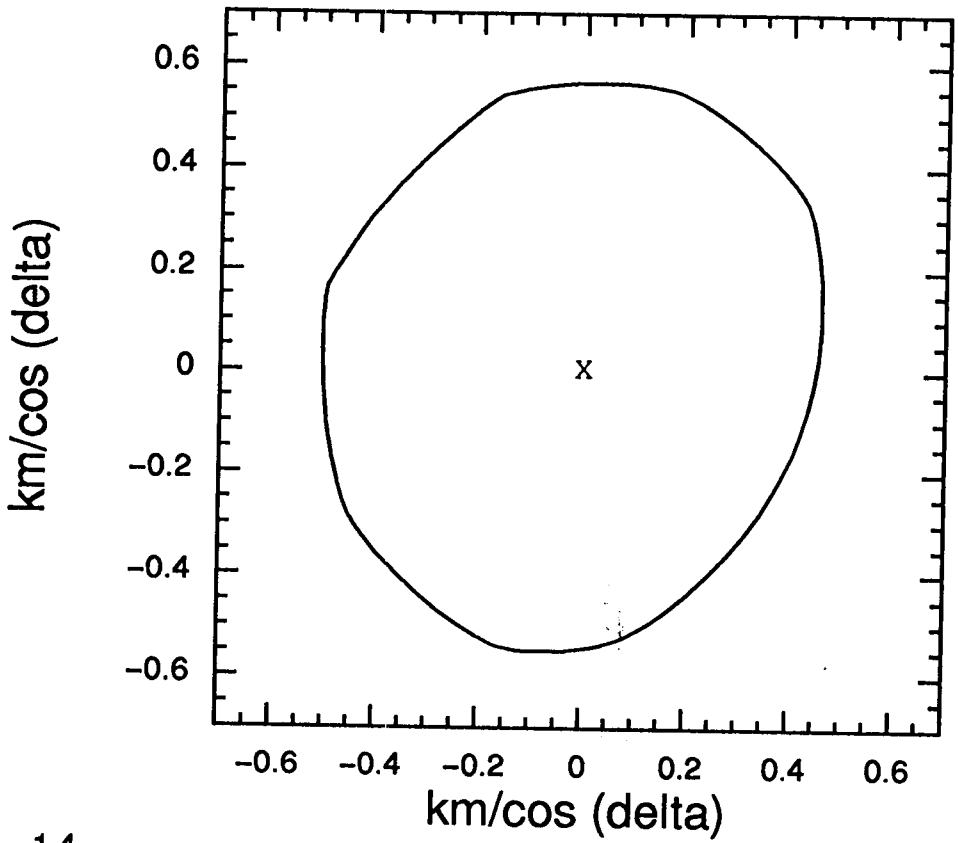

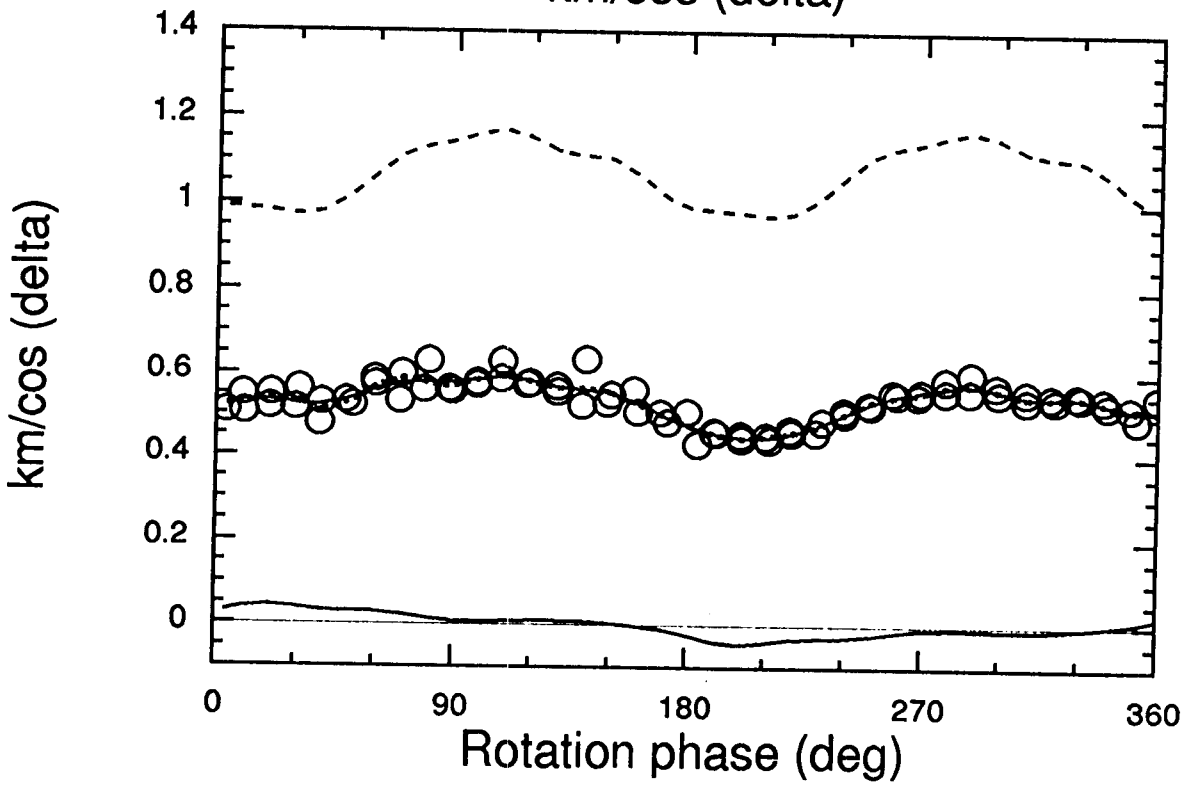

cs240hull.tpl

6.17.98

AUGUST 28

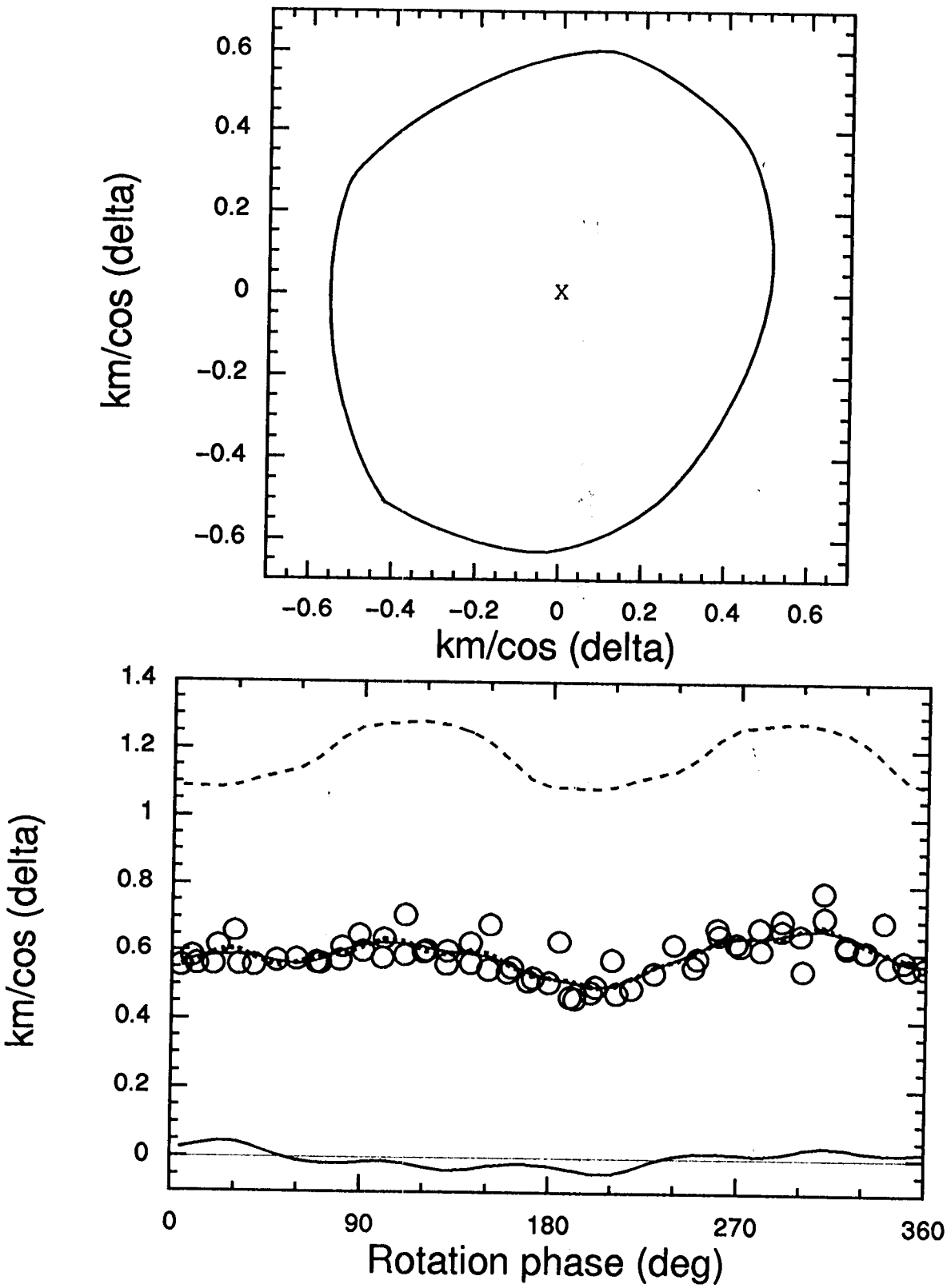

cs241hull.tpl

6.17.98

AUGUST 29

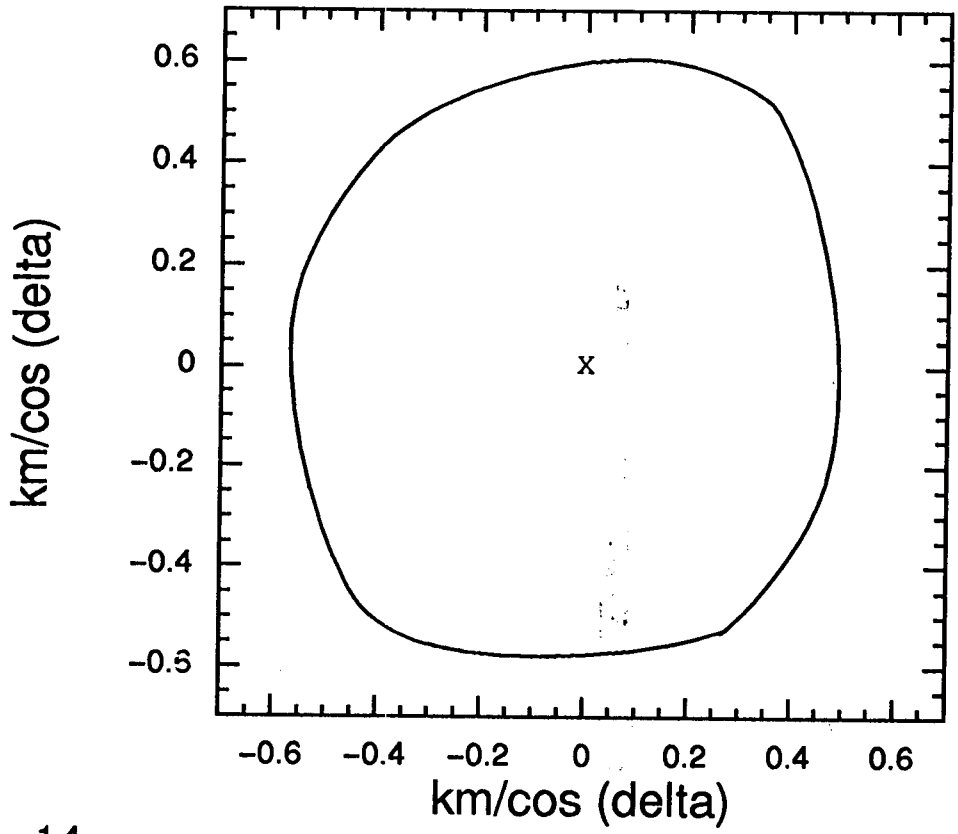

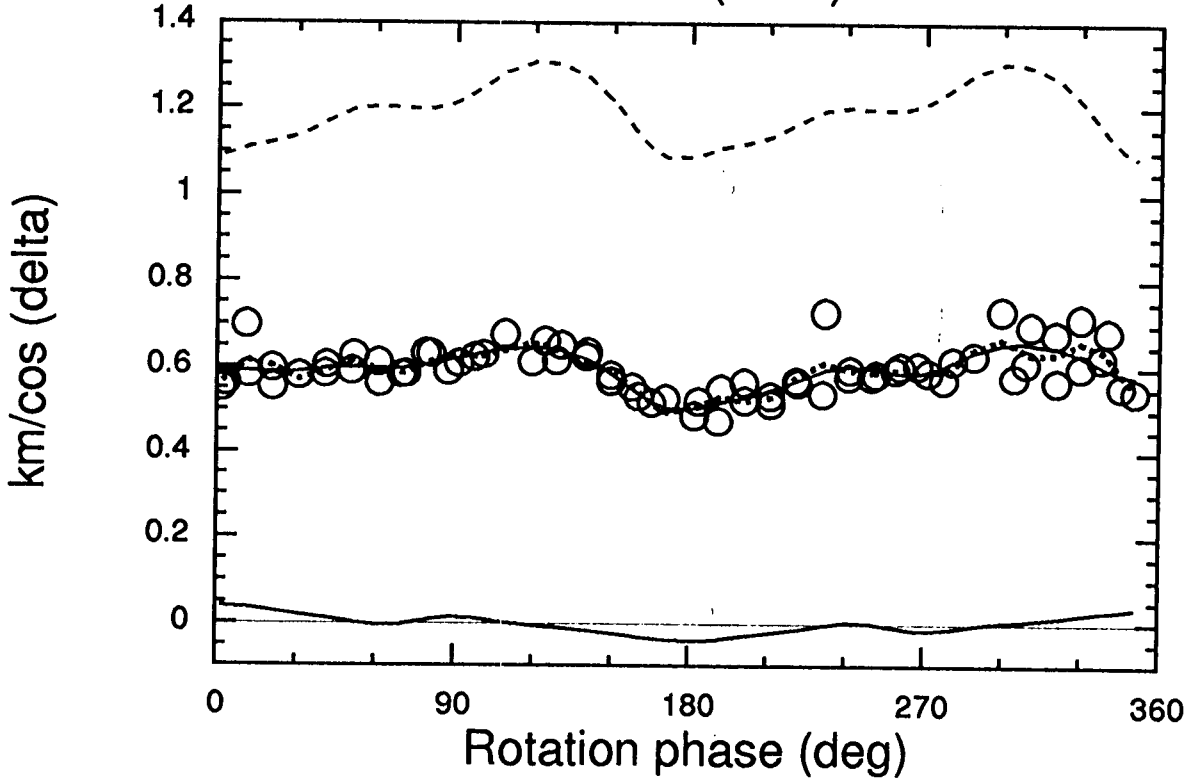

cs242hull.tpl

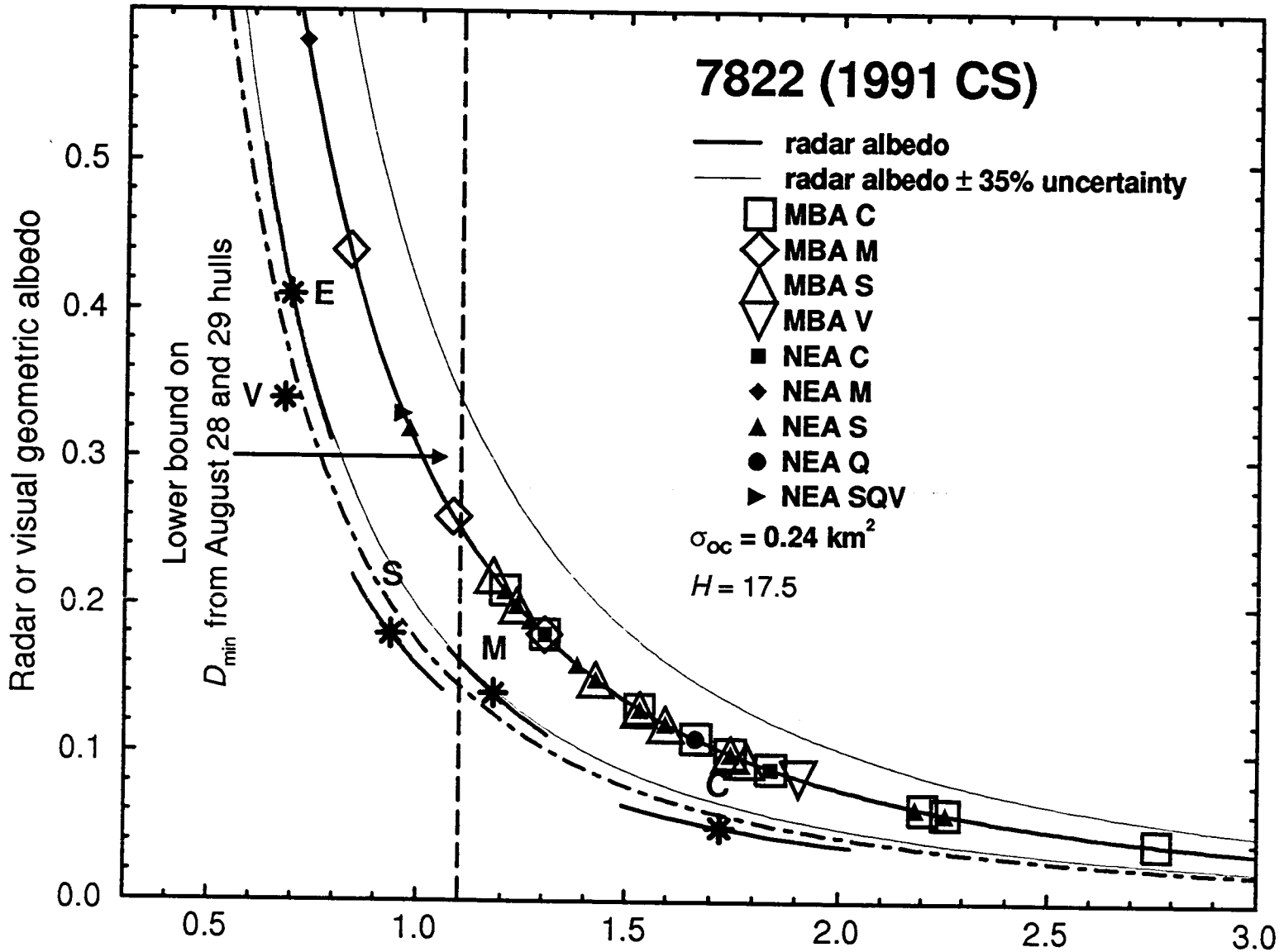
7822 (1991 CS)
radar albedo
radar albedo ± 35% uncertainty
MBA C
MBA M
MBA S
MBA V
NEA C
NEA M
NEA S
NEA Q
NEA SQV
σ_{oc} = 0.24 km^2
H = 17.5
Lower bound on
D_{min} from August 28 and 29 hulls
E
V
S
M
C
Radar or visual geometric albedo
Effective diameter or D_{max} (km)
0.0
0.1
0.2
0.3
0.4
0.5
0.5
1.0
1.5
2.0
2.5
3.0

Fig. 10